Increasing Photon Collection Efficiency for Generating Long-distance Entanglement of Atoms

Timon Fabian Hummel

München 2018

Increasing Photon Collection Efficiency for Generating Long-distance Entanglement of Atoms

Timon Fabian Hummel

Masterarbeit
an der Arbeitsgruppe von Prof. Dr. Harald Weinfurter
der Ludwig–Maximilians–Universität
München

vorgelegt von
Timon Fabian Hummel
aus Freiburg

München, den 02.10.2018

Steigerung der Aufsammeleffizienz von Photonen zur Erzeugung von Verschränkung zwischen Atomen über lange Distanzen

Timon Fabian Hummel

Masterarbeit
an der Arbeitsgruppe von Prof. Dr. Harald Weinfurter
der Ludwig–Maximilians–Universität
München

vorgelegt von
Timon Fabian Hummel
aus Freiburg

München, den 02.10.2018

Contents

1. Introduction

At the beginning of the 20th century, puzzling physical phenomena for example the black body radiation or the photoelectric effect couldn't be explained by any available theory and weren't in agreement with the classical laws of physics. This made it obvious, that the state of the science and the fundamental understanding of the world needed revision. During the development of quantum mechanics it became apparent that these problems could only be solved by leaving behind the classical and intuitive picture of nature, but allowing for radically different approaches in the conceptual and mathematical sides. One of the new properties of quantum mechanics was entanglement, which gives rise to effects which Einstein called "spooky action at a distance"[11]. Entangled particles have the special feature that their quantum state can't be described independently of each other. In fact, particles that interacted with each other retain a type of connection which correlates any measurement results of one of the particles immediately to the result obtained from the other particle. Einstein, Podolsky and Rosen argued against the completeness of quantum mechanics in their famous EPR-paradox paper in 1935 [12]. In this paper they demand that every physical theory must adhere to unique properties. First is the concept of locality which means that separated events can't influence each other faster than with the speed of light. Further, they required completeness of the theory, i.e. that it is in agreement with any physical experiment. The last property is the concept of realism, which demands that a physical system must have a distinct state and measurement result before it is measured and can't be defined by the measurement process itself. Hence, the riddle of quantum mechanics in their postulate could only be solved if it contained what was later called local-hidden-variables (LHV). However, in the 1960s, John Bell proposed a theorem that could rule out the LHV postulate for quantum mechanics [3] . In that work, Bell argues that the statistical predictions of quantum mechanics are in contradiction with that of a local realistic theory. This discrepancy is expressed in his famous inequality, which gives an upper limit for correlation measurements on two spin $\frac{1}{2}$ particles predicted by local realistic theories. Later, Clauser, Horne, Shimony and Holt (CHSH) formulated an alternative inequality for testing Bell's theorem in order to test the possibility of the existence of local hidden variables [10]. By now, it was possible to test Bell's inequalities in several experimental schemes including some with closing of all essential loopholes [16, 13, 8, 23]. These experiments indicated strong evidence against the existence of LHV theories and hence led to the conclusion that no local realistic extension for quantum mechanics is possible.

Besides the fundamental and philosophical controversy about the concept of entanglement, the properties of quantum states gave rise to new fields of research such as quantum information and communication theory. The vision behind a large quantum communication network is to enable the transmission of quantum information - in form of a quantum state - between any two physi-

cally separated points which would allow for the application of distributed quantum computing and secure quantum communication [1, 18, 4] Compared to a classical computer, a quantum computer has the potential to solve a certain type of problems more efficiently by using quantum entanglement and secure quantum communication provides unconditionally secure exchange of information between two nodes which often relies on the properties of entanglement. The general structure of a quantum network consists of numerous nodes each containing a quantum memory. Further, it is required to have channels between the nodes over which the information can be transmitted. The transmission of the quantum information between the quantum memories is done by photons which can be sent over long distances with little decoherence.

The setup in this work represents the most simple form of a quantum network which consists of two nodes which are connected by a quantum channel. The nodes are located in two laboratories which are separated by 400 m distance and 700 m fiber link. In each of the labs we trap a Rubidium 87 atom which represents the quantum memory. In order to create entanglement between the two nodes, which is impossible for atoms in a direct interaction, we establish entanglement in each lab between the spin of the atom and the polarization state of a photon from a spontaneous emission process of the atom. For eventually entangling the atom-atom pair, we make use of the so called entanglement swapping protocol [28] which allows to create entanglement between two arbitrary physically separated particles. This is done by sending the photons to a measurement setup which projects them onto a maximally entangled Bell-state. In consequence the atoms are themselves projected onto an entangled state.

An important requirement for quantum networks is to achieve a large distance between the nodes. However, increasing the distance brings several difficulties as for example the preservation of the coherence time of the atomic state and the transmission losses of the photons in the optical fibers. Moreover, the rate for generating atom-atom entanglement in schemes based on entanglement swapping is also limited by the efficiency for collecting the photons from the quantum memories. The main challenge for the collection efficiency is the performance of the collection optics. In our experiment we employ a high NA microscope objective to collect photons from the spontaneous emission process of an atom and couple them into a single mode fiber. Due to the bad performance of the currently used collection optics which is in particular not diffraction limited for the wavelength of the photons, allows for only less than 1% of all emitted photons to be used in our experiment.

This work presents an upgrade of the photon collection setup with a new high NA custom designed microscope objective. In the beginning this work gives an overview of the current experiment and the general theory for creating atom-atom entanglement by using an entanglement swapping scheme. The following chapter discusses the general atom-atom entanglement event rate generation for the experiment and points out limitations of the current setup for achieving even longer distances of entanglement. Chapter 4 contains calculations on the coupling efficiency of photons which are emitted by the trapped atom into a single mode-fiber. This is done for two cases, a simplified approach considering unpolarized photons and a full treatment which includes the dipole emission characteristics of the quantum memory. The final chapter presents the experimental details for the new microscope objective setup regarding used optical elements and techniques for aligning the setup.

2. Overview of the experiment

Achieving long-distance atom-photon entanglement as well as atom-atom entanglement is a complicated process involving several experimental steps. In the following chapter I will describe the current scheme for the generation of entanglement over a distance of 700m fiber and 398m spatial separation as well as the involved techniques. This scheme was developed over the last 17 years and eventually lead to a statistically significant, event-ready Bell test closing all essential loopholes, namely the detection and locality loophole [23].

2.1. Atomic system - Rubidium 87

The atom used in this experiment is Rubidium 87. This choice has several reasons. ^{87}Rb is an alkaline metal and therefore only has one valence electron. The level structure and its properties are thoroughly understood and its transitions accessible by existing commercially available laser systems. The atomic ground state is $5S$ and the first excited state excited state $5P$. Due to the fine structure induced by the electron spin, the first excited state splits into two sub-levels $5^2P_{3/2}$ and $5^2P_{1/2}$. Further, ^{87}Rb has a nuclear spin of $I = \frac{3}{2}$ which additionally splits the ground state into the hyperfine structure levels $5^2S_{1/2}$ $F = 1$ and $5^2S_{1/2}$ $F = 2$ and the excited states in $F' = 1, 2$ $(5^2P_{1/2})$ and $F' = 0, 1, 2, 3$ $(5^2P_{3/2})$ respectively. The hyperfine structure sub-levels in turn consist of $2F+1$ Zeeman sublevels which are denoted for the ground state as F with $|F, m_F\rangle$ and as F' with $|F', m_{F'}\rangle$ for the excited state. The qubit used in the experiment consists of the Zeeman sublevels $|F = 1, m_F = +1\rangle$ and $|F = 1, m_F = -1\rangle$ of the ground state. Together with $|F' = 0, m_F = 0\rangle$ of the excited state, this forms a so called Λ-system which is beneficial for the employed entanglement scheme and will be discussed in a later part in more detail.

2.2. Trapping single atoms

Experiments on single atoms require a precise and stable localization of the atom for a certain time along with a good isolation from its environment. In our experiment this is achieved by using an ultrahigh vacuum (UHV) which is able to achieve pressures of about 10^{-10} mbar. A glass cell is attached to the main part of this UHV-setup, containing a metal vapor dispenser which evaporates Rubidium atoms when it is heated. Inside the glass cell the atoms are trapped with an

optical dipole trap (ODT) which has a trapping potential in the order of $k_B \cdot 1$ mK. However, in order to successfully trap the atoms an additional cooling step is required. A magneto optical trap (MOT) is used to cool the atoms close to or even below the Doppler limit, which makes it possible to load the atoms into the ODT. The following chapter will explain the trapping mechanism used in the experiment in further detail.

2.2.1. Optical dipole trap

A simple way for trapping cold atoms is to use a single tightly focused TEM_{00} Gaussian beam, creating an attractive potential for the atoms. The underlying effect of this attractive potential is the AC-Stark shift. A laser beam that is far detuned to a transition between a ground and an excited state will shift the ground state by:

$$\Delta E_g = \frac{\hbar \Omega^2}{4\delta} \sim \bar{I}$$

where Ω is the on-resonance Rabi-frequency, $\bar{I}$ the average intensity of the light field and $\delta = \omega_A - \omega_L$ the detuning, i.e the difference between the atomic transition frequency and the frequency of the laser used for the dipole trap. For a far red detuned laser ($\delta > 0$) the energy level of the ground state is lowered which results in an attractive potential for the atom. The spatial dependency of this energy shift is given by the intensity distribution of the Gaussian beam. For a beam propagating in z-direction, the distribution is given by:

$$I(r, z) = I_0 \frac{2}{\pi w_0^2} \cdot e^{-\frac{2r^2}{w_0^2}} \tag{2.1}$$

Where I_0 denotes the intensity at the position $r = 0$ and $z = 0$ and w_0 is the minimal transversal size of the Gaussian beam waist. At a general position z along the beam, the local waist size behaves according to:

$$w(z) = w_0 \sqrt{1 + \left(\frac{z}{z_R}\right)^2}$$

where

$$z_R = \frac{\pi w_0^2}{\lambda}$$

is the so called Rayleigh length. Concerning the ^{87}Rb atom used in our experiment, the atomic sublevel structure is more complex involving several transitions. Thereby, the dipole potential in general depends on the specific sub-state of the atom. But whenever the optical detuning is large compared to the hyperfine splitting of the excited states, the following equation for the trap depth holds for the respective Zeeman state[14]:

$$U_{dip}\left(\overrightarrow{r}\right) = \Delta E = \frac{\pi c^2 \Gamma}{2w^3} \cdot \left(2 + \frac{Pg_F m_F}{\Delta_{2,F}} + \frac{1 - Pg_F m_F}{\Delta_{1,F}}\right) \cdot I\left(\overrightarrow{r}\right) \tag{2.2}$$

Here g_F is the atomic Landé factor of the respective Zeeman-state m_F, Γ the spontaneous scattering rate, w the resonance frequency, $\Delta_{1,F}$, $\Delta_{2,F}$ the detunings of the light field to the D_1 and D_2 lines and P the polarization of the light ($P = 0$ for linear polarization and $P = \pm 1$ for circular polarization). An example for a trapping potential created by a focussed TEM_{00} Gaussian beam is shown in figure 2.1.

If the thermal energy $k_B T$ is much smaller than the trapping potential U_{dip}, the dipole potential can be well approximated by a simple cylindrically symmetric harmonic oscillator [27]. In that case the oscillation frequencies of a trapped atom are given by:

$$\Omega_r = \sqrt{\frac{4U_0}{mw_0^2}}$$

$$\Omega_z = \sqrt{\frac{2U_0}{mz_R^2}}$$

where m is the mass of the atom, Ω_r the trapping frequency in radial direction and Ω_z the trapping frequency along the axis of the beam direction. The trap geometry, together with the cooling light leads to the so called "collisional blockade"-effect [24]. For a trap volume that is small enough, collisions of excited atoms become the dominant mechanism for atom losses, whereby the atom number will be reduced until there is only one atom left in the trap.

The influence of the trap geometry and the impact of the thermal atom motion inside the trap on the photon collection efficiency will be discussed in more detail in Chapter 4.

2.2.2. Magneto optical trap (MOT)

In order to trap an atom in the optical dipole trap, the kinetic energy of the atom has to be sufficiently small, i.e. smaller than the conservative trapping potential of the dipole trap. The reduction of the kinetic energy will be done by radiation pressure using the Doppler effect [15, 9]. The principle is the absorption and subsequent spontaneous emission of photons. The momentum transfer by the absorption is directed in the propagation of the photon whereas the momentum transfer of the spontaneously emitted photon is isotropic. When this is done by using red detuned laser beam which hit the atom cloud from 6 directions, it results in an effective velocity dependent force which eventually deccelerates the atoms. The minimal temperature for Rubidium atoms by using Doppler-cooling is $146\mu m$. The cooling light in our experiment is red detuned to the closed transition $5^2 S_{1/2} |F = 2\rangle \rightarrow 5^2 P_{3/2} |F' = 3\rangle$. In addition, we use a repump beam which is resonant to the transition $5^2 S_{1/2} |F = 1\rangle \rightarrow 5^2 P_{3/2} |F' = 2\rangle$ and which has the purpose
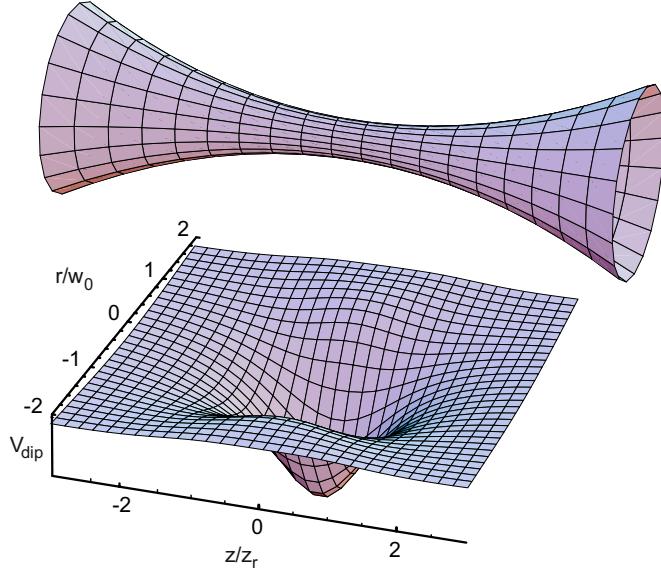
Figure 2.1.: Schematic drawing of a focussed TEM_{00} gaussian beam and the corresponding trapping potential [27].

to put the atoms decaying to the $5^2S_{1/2}\,|F=1\rangle$ state back into the cooling cycle. In order to not only have a velocity dependent dissipative force but also a position dependent force, a magnetic quadrupole field is generated by coils in anti-Helmholtz configuration around the vacuum cell. The magnetic field gradient causes a position dependent shift of the atomic Zeeman states. Together with appropriate polarization of the cooling beams this results in a velocity dependent cooling mechanism which additionally leads to spatial confinement.

2.3. Atom-Photon entanglement

In our experiment, the requirement for creating entanglement between two atoms is first of all to create independent atom-photon entanglement in two separate traps. As the way to create atom-photon entanglement is similar in both traps, the following part will describe the experimental scheme for atom-photon entanglement in one of the two traps.

The trapped single Rb^{87}-atom will be prepared in the $5^2P_{3/2}\,|F'=0\rangle$ state. Now, the atom can spontaneously decay in the three different states $5^2S_{1/2}|F=1,m_F=-1\rangle$, $|F=1,m_F=0\rangle$ and $|F=1,m_F=+1\rangle$ (see figure 2.2). Due to angular momentum conservation, the spin of the emitted photon is $|\sigma^+\rangle\,|\sigma^-\rangle$ or $|\pi\rangle$ which corresponds to left circular, right circular and linearly polarized light. The spatial modes of $|\pi\rangle$- and $|\sigma^{\pm}\rangle$-polarized light differ from each other since electromagnetic radiation is a transverse oscillating wave [26]. The probability of the atom emitting into a certain spatial mode is given by the emission characteristics of the dipole
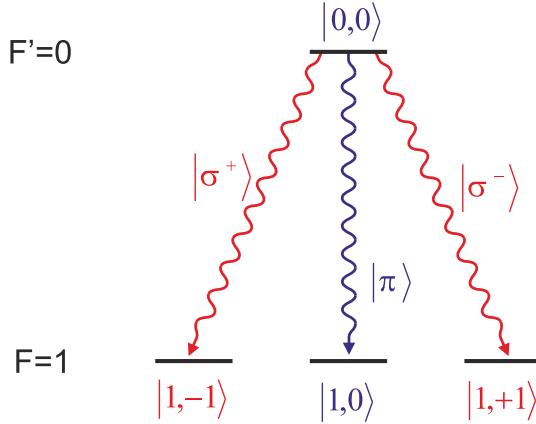
Figure 2.2.: Atom-photon entanglement scheme. Spontaneous decay of the excited state $5^2P_{3/2}\,|F'=0, m_{F'}=0\rangle$ via either emitting a $|\sigma^+\rangle$ or $|\sigma^-\rangle$ polarized photon. The π polarized light to the $|F=1, m_{F'}=0\rangle$ state is automatically filtered out due to the orientation of the quantization axes[26].

radiation [17]. The spatial dependence of emission of $|\pi\rangle$- and $|\sigma^\pm\rangle$-polarized light is shown in figure 2.3. Here, the z-direction denotes the quantization axis. The emission into the spatial mode is dependent on the angle θ relative to the quantization axis. The probability to emit π-polarized light scales with $\sim \sin\theta$ and thereby no π-polarized photon is emitted into the quantization axis. However, for $\sigma^\pm$-polarized light the intensity scales with $\sim 1 + cos\theta$ and hence has a maximum probability to be emitted along the quantization axis. Since the microscope objective collecting the photons in our experiment defines the optical axis and thereby the quantization axis, in theory no π-polarized light will be collected during the experiment. This is not the case if the position of the atom and thereby the emission is shifted from the quantization axes. This effect will be investigated in Chapter 4.2. However when leaving out these effects and analyzing the emission at the quantization axis we obtain for the final atom-light system the following maximally entangled state of the atomic qubit and the polarization state of the emitted photon:

$$|\Psi\rangle = \frac{1}{\sqrt{2}} \left(|\sigma^+\rangle\,|1, -1\rangle + |\sigma^-\rangle\,|1, +1\rangle \right) \tag{2.3}$$

2.3.1. Atomic state readout

For the atomic state readout a novel approach was developed [19] in order to fast and efficiently detect and analyze the state of the atom, which is a prerequisite for the verification of atom-photon and atom-atom entanglement. The procedure for the atomic state readout consists of

(a)

(b)
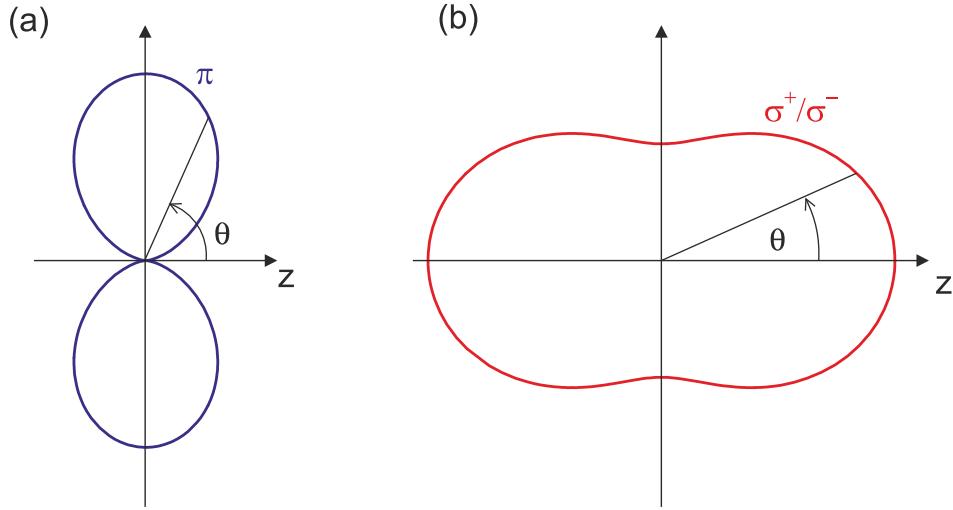
Figure 2.3.: Dipole emission characteristics of a) π- and b)$\sigma^{\pm}$-polarized light. The emission intensity is dependent on the angle θ relative to the quantization axis. There is no emission of π-polarized light in z-direction whereas $\sigma^{\pm}$-polarized emission in this direction is maximal [26].

two main steps. At first, the atom whose state is within qubit subspace $\{|1,-1\rangle, |1,+1\rangle\}$ is excited by a so called readout laser $\left(5S_{1/2}F = 1 \rightarrow P_{1/2}F' = 1\right)$ with a fixed polarization, which is either $|\sigma^+\rangle$ or $|\sigma^-\rangle$. Depending on the atomic state, only a certain superposition of the states will be excited by the readout laser due to transition selection rules. For example a $|\sigma^+\rangle$ polarized readout laser would excite the $5^2S_{1/2}|1,-1\rangle$ state but would leave the $5^2S_{1/2}|1,+1\rangle$ state unaffected, since the corresponding excited state $|5^2P_{1/2}, F' = 1, m_F = +2\rangle$ doesn't exist. The one state that gets excited is called "bright state" ($|\Psi\rangle_B$) and the orthogonal unaffected state is called "dark state" ($|\Psi\rangle_D$). If the lifetime of the excited state was too short, i.e. it decayed before the ionization to the $5^2S_{1/2}F = 2$ state, the atom can't be ionized anymore. Therefore, we use a so called Cycling-Laser ($780nm$) which re-excited the atom from the $5^2S_{1/2}F = 2$ to the $5^2P_{3/2}F' = 3$ state from which it can be ionized again (see figure 2.4) .

The second step for the atomic state readout is ionization by a simultaneously applied laser pulse at 473 nm. The duration and success probability for the ionization is dependent on the power of the laser beam. After the state selective ionization of the atomic state, the ionization fragments are detected by two so called Channel Electron Multipliers (CEMs). The ionization fragments, being an ion and an electron, are accelerated towards the CEMs by applying a strong electric field. Once they hit the active area of the CEMs secondary electrons are released which are amplified within an avalanche which, in turn is then amplified and leads to a small current pulse. If either the electron or the ion will be detected it is thereby possible to determine whether the atomic state was in the bright- or dark state. The combined detection efficiency of the CEMs for detecting one of the two ionization fragments (electron or ion) is $\eta \gtrsim 0.98$. The performance of the state-selective ionization can be described by the ability to distinguish between dark and bright state which we call contrast. It is given by the probability to correctly detect the atoms in
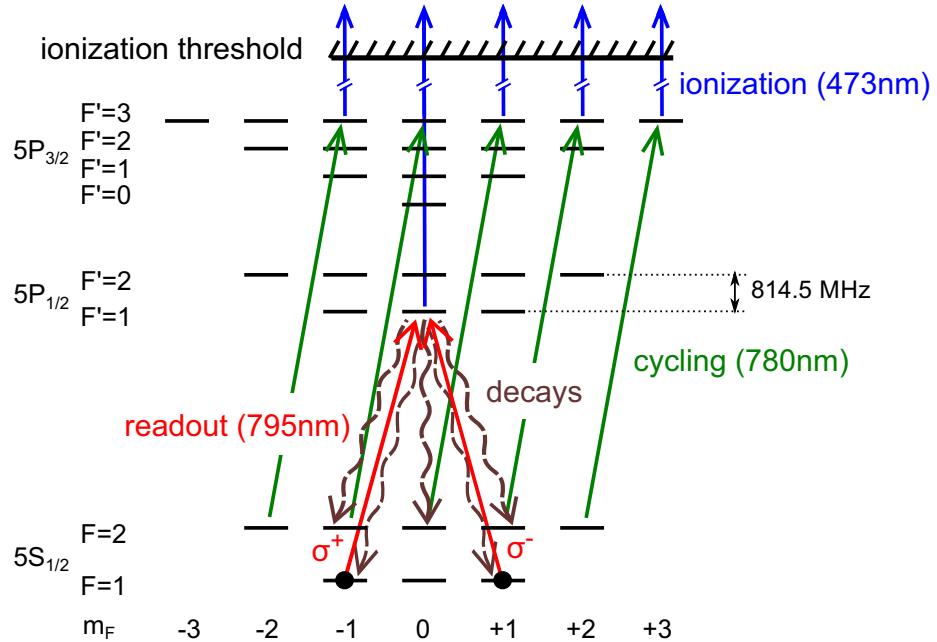
Figure 2.4.: Atomic state readout scheme. The polarization of the readout laser determines whether the atomic state gets excited and subsequently ionized. This process is called Zeeman state selective ionization. Additionally, the cycling laser re-excites atoms which decayed before the ionization [19].

the dark state minus the probability for wrong detection in the bright state. The resulting contrast that is achieved in the state-selective ionization scheme is 93.8%.

2.3.2. Entanglement swapping

In order to generate atom-atom entanglement between separate atoms we employ the entanglement swapping protocol [28]. Starting with two independent and spatially separated entangled atom-photon pairs it is possible to achieve atom-atom entanglement without any direct interaction between the two atoms. The basic principle of entanglement swapping is based on a joint Bell-state measurement of the photons which projects them onto an entangled state. In our experiment this is realized by two-photon-interference at a fiber beam splitter. After that, the polarization of the photons is measured by using polarizing beam splitters and avalanche photo diodes which swaps the entanglement of the atom-photon pair into an entanglement between photon-photon and atom-atom. For this scheme it is crucial to have indistinguishable photons, i.e. they must be in the same quantum state concerning all degrees of freedom except for polarization. Since the origin of the photons in our case is the same atomic transition and the excitation scheme is synchronized we are able to ensure a spectral and temporal mode overlap of the photons close to unity. An overview of the scheme is depicted in figure 2.5.

From this it follows that the atom-atom entanglement scheme can only successfully be employed if there are two independent and timed entangled atom-photon pairs in the first place. Therefore, every change of generation efficiency of these pairs will have immediate impact on the overall event success probability. Critical parameters are for example the transmission losses in fibers, detection efficiency of the detectors and especially the collection efficiency of the spontaneously emitted photons. The success probability for atom-atom entanglement will further be reduced when aiming for even longer distances than the one currently achieved.

The following chapter will point out the limitations of the current setup for achieving the goal of increasing the entanglement distance from 400 m up to 20 km. Further, the approach for realizing long-distance entanglement by implementing a high NA microscope objective is introduced.
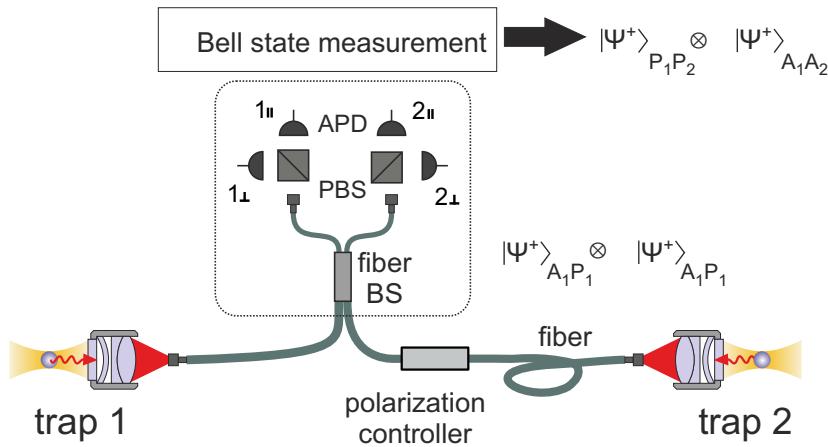
Figure 2.5.: Sketch of the atom-atom entanglement scheme. The basic principle is to create atom-photon entanglement in two separate traps, followed by a coincidental Bell state measurement (Coincident detection of two photons). This leads according to the entanglement swapping protocol to atom-atom entanglement without any direct interaction.

3. Towards long-distance entanglement between atoms

After successful demonstration of entanglement of atoms separated by 400 m, the next step towards other applications, such as quantum networks would be to significantly extend the distance between the two entangled atoms. However, increasing the distance will have drastic impact on the generation rate of atom-atom entanglement in our experiment. The reasons for that and possible upgrades for the setup will be discussed in this chapter.

3.1. Generation rate of remote atom-atom entanglement

For possible future applications of entangled atomic quantum memories such as distributed quantum computing or secure quantum communication, it will be necessary to extend the distance between the atomic memories. So far, in the frame of the experiment, we were able to create atom-atom entanglement over a distance of 400 m and 700 m fiber length. The increase of the distance between the entangled atom-atom pair gives rise to several difficulties. One of the problems at longer distances is the small rate of generating remote entanglement in schemes based on entanglement swapping. Currently, the event rate is determined by several factors which are mainly:

- The photon detection efficiency by the avalanche photo diodes

- Transmission losses in the optical fibers

- Photon collection efficiency from the quantum memory

- The propagation time of the signal

The generation rate for atom-atom entanglement can be calculated as the product of the success probability P_s of coincidental atom-photon entanglement and the repetition rate f_e of an atom-photon entanglement attempt. The sequence of such an attempt and the corresponding time lengths for the current setup are depicted in figure 3.1.
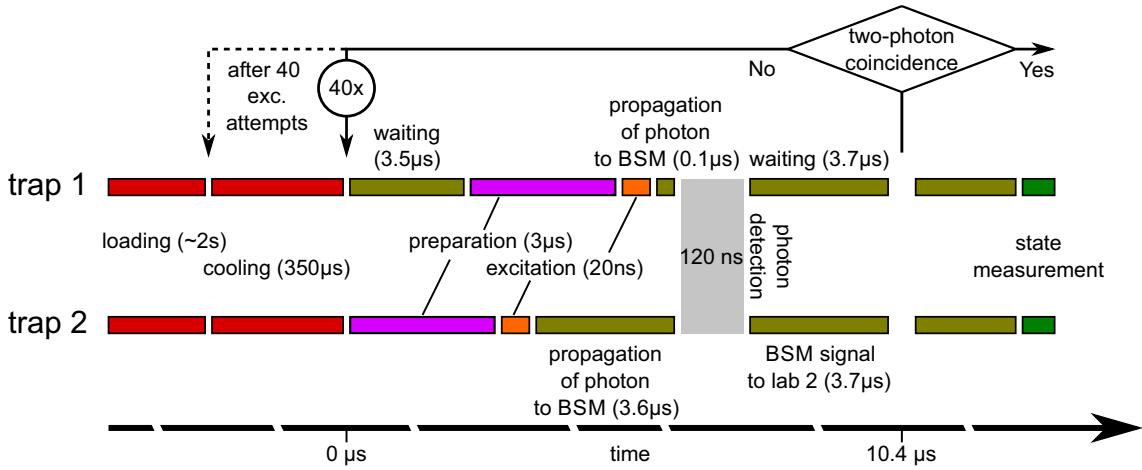
Figure 3.1.: Experimental sequence and timings to entangle two Rubidium atoms in two separate traps. Once there are two atoms loaded in both dipole traps, the previously described pumping and excitation scheme is repeated until successful atom-photon entanglement in both traps is achieved. Each excitation cycle will heat the atom hence there will be a cooling period after 40 excitation repetitions [7].

The event rate can then be estimated as:

$$R_e = f_e \cdot P_s \simeq \frac{1}{2} \cdot \frac{1}{\frac{350\mu s}{40} + 3\mu s + \frac{2d}{\frac{2}{3}c}} \cdot \eta_{col}^2 \cdot \eta_{det}^2 \cdot \tau_{fiber} \tag{3.1}$$

where $350\mu s$ is the time needed for cooling the atom again after a repetition of 40 excitation cycles. The atom in the trap is heated during the preparation-excitation cycles where it scatters many photons of the pumping excitation beams and hence needs to be cooled again. The 3 μs yield from the preparation of the atom in the $5^2 S_{1/2} F = 1 |m_F = 0\rangle$ state. The Bell state measurement is in one of the labs, thus the photon and the success signal together take the distance $2d$, where d is the distance between the two labs with a propagation speed of $\frac{2}{3}c$ in the optical fiber.

The other part that determines the event rate for a successful atom-atom entanglement event is the success probability. It is dependent of the collection efficiency n_{col}, which is a measure for the fraction of photons that can be collected by the objective during the spontaneous emission of the atom, the transmission through the optical fiber τ_{fiber} and the photon detection efficiency n_{det} of the avalanche photo diodes. n_{col} and n_{det} both enter quadratically since for a successful atom-atom entanglement event, it is necessary to have a successful atom-photon event in each of the two traps in the first place. Hence, for a successful event we need to collect two photons and detect two photons during the BS-measurement.

The current experimental setup yields around two events per minute with 700m fiber length between the two traps. The fiber length distance we are aiming for is in the order of 20km.

The photon collection efficiency is currently in the order of $\eta_{col}^2 = 0.92\%$ and the absorption in optical fibers at a wavelength of 780nm is $3.5\frac{dB}{km}$. As shown in figure 3.2 the event rate drops exponentially with the fiber length and we estimate to get one event per year at 20 km distance. This makes the current setup unsuitable for long-distance entanglement. However, there are several improvements possible in order to enable long-distance entanglement at a reasonable event rate.
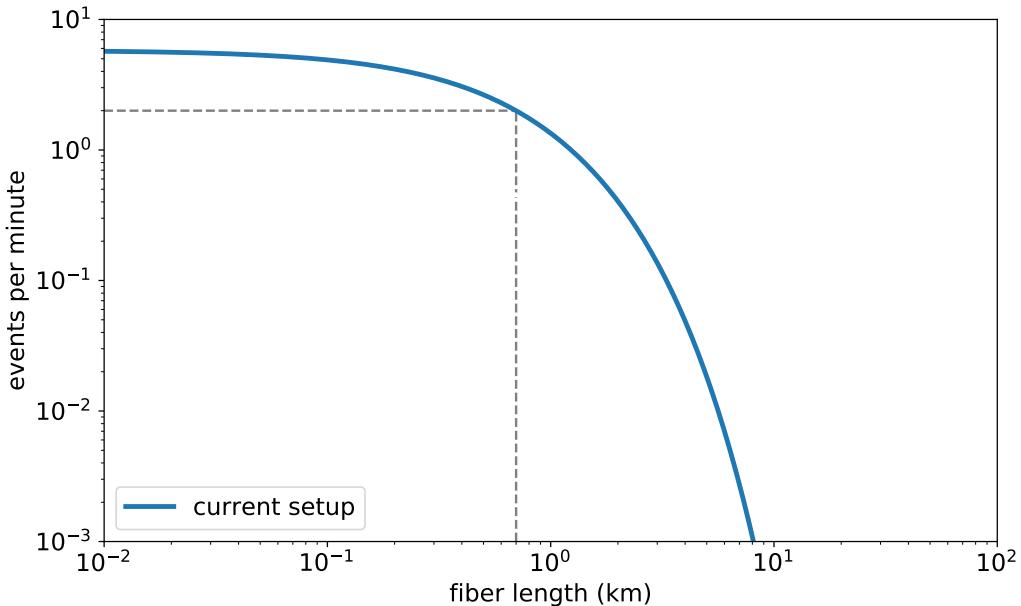
Figure 3.2.: Events per minute for the current setup with a photon wavelength of 780nm. The gray line shows the current length of the optical fiber with $700m$ which yields around 2 atom-atom entanglement events per minute.

3.2. Photon conversion to the telecom band

The Rb atomic quantum memory we use in the experiment as a quantum storage system has the advantage of having a long coherence time and its transitions accessible by existing commercially available laser systems. However, the main disadvantage that makes it less suitable for long-distance entanglement is the optical transitions being in the near infrared. The attenuation of light propagating through an optical fiber strongly depends on the wavelength. There are several processes connected to possible loss mechanism in fibers, which are mainly:

- Rayleigh scattering, which is the dominant process for wavelengths in the visible regime. The basic principle is that light scatters on material inhomogeneities which are smaller than the wavelength. The losses scale with $\sim \frac{1}{\lambda^4}$.
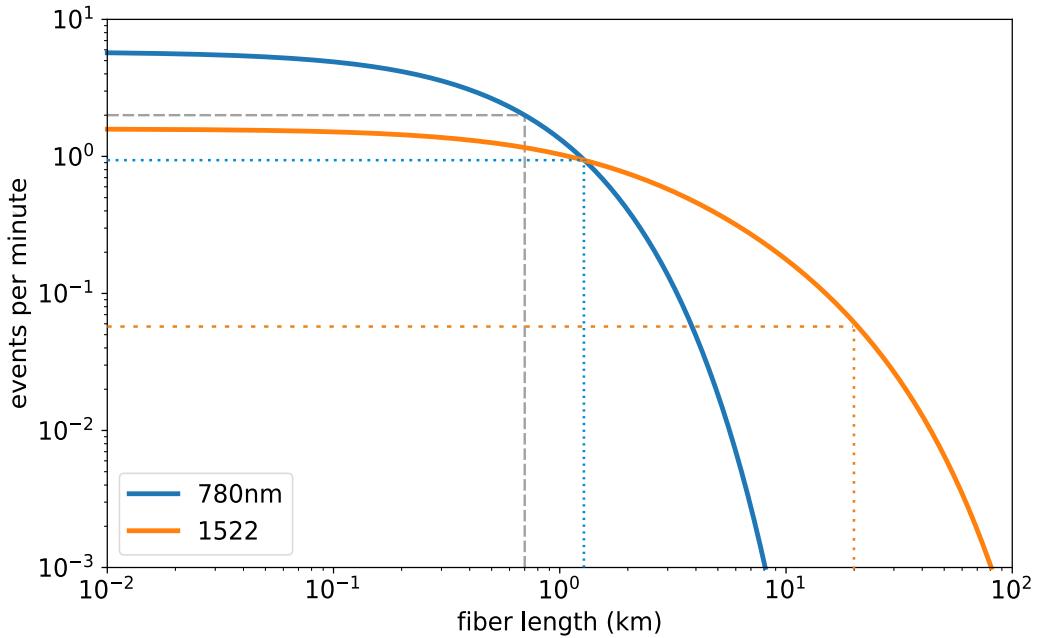
Figure 3.3.: Events per minute at wavelengths 780nm and 1522nm. The grey dashed line shows the current event rate at a distance of 700m. The blue dotted line shows the point from which the conversion to 1522nm pays off (40% photon conversion efficiency, 80% photon detection efficiency) which is after 1.5km. At a fiber length of 20km with photons in the telecom band one obtains $\simeq 0.06$ events per minute which is marked by the orange line.

- Absorption, which is caused by the conversion of electromagnetic wave energy into other forms of energy, f.e lattice vibrations and occurs at wavelengths > 1600 nm

- Material impurities, which lead to absorption losses. The most important impurity in modern optical fibers is induced by water in form of hydroxyl ions.

However, there is a promising regime with minimal attenuation, which is in the so called telecom band at $\simeq 1550$ nm. Here the losses are $0.2\frac{dB}{km}$ (1522 nm) compared to $3.5\frac{dB}{km}$ for the current 780 nm photon wavelength. By adapting the approach in [5], where they demonstrated the conversion of photons emitted by trapped ions to the telecom band, we intend to convert the photon emitted from our Rb quantum memory at a wavelength of 780nm to the telecom band at 1522nm. It has been shown that the non classical properties of the single photons, especially the polarization and indistinguishability are preserved. The external conversion efficiency is expected to be as high as 40%. The other advantage in the telecom band is that it becomes possible to use superconducting single photon detectors (SSPD) which are specified to have a photon detection efficiency n_{det} of 80%, compared to the currently used avalanche photo diodes which have an efficiency of 40%.

Figure 3.3 depicts the estimated event rate over distance after the telecom conversion assuming a

conversion efficiency of 40% and photon detection efficiency n_{det} of 80%, compared to the event rate at 780 nm and 40% photon detection efficiency. The losses of the conversion are compensated by lower attenuation after a distance of 1.5 km, which is represented by intersection of the two solid plotted lines. At a fiber length of 20 km the converted photons yield an estimated event rate of $\simeq 0.06$ events per minute.

This would already be a significant improvement compared to the current setup, yet this event rate still wouldn't yield high enough statistics for feasible atom-atom entanglement over long distances. Further improvement towards long-distance entanglement has to be achieved by increasing the photon collection efficiency from the atomic quantum memory.

3.3. High NA microscope objective

As discussed in Chapter 2, a microscope objective is used for confocally focusing the dipole trap, the ionization laser beam and for collecting the spontaneously emitted entangled photons. Currently, we use a standard commercial objective (Mitutoyo G Plan Apo 50) with a numerical aperture (NA) of 0.5 which is corrected for the 3.5 mm glass wall between the objective and the focal spot. The numerical aperture of an optical system is a measure for the angle under which the objective can collect light or emit light. It is given by:

$$NA = n \cdot sin\left(\theta\right) \tag{3.2}$$

where θ is the half angle of the cone that can enter or exit the objective and n the refractive medium in which the objective is imaging. Even though the objective is specified for a diffraction limited imaging up to an NA of 0.5, this is only the case in the visible regime. As the objective is not diffraction limited for the wavelength of the fluorescence collection, only a small part of the full aperture can be used for coupling into a single-mode fiber without being limited by aberrations. In general, it is important for the photon collection efficiency to distinguish between the collection of the photons by the objective and the coupling of the collected photons into a single mode fiber.

- The *photon collection* is determined by the ability of the objective to collect photons of the atom in the trap. It is dependent on the possible diameter of the focal spot for the fluorescence collection and hence the beam size of the respective collimator.

- The *photon coupling* into the single mode fiber, i.e. the fraction of the collected photons that are coupled into the single-mode fiber and hence can be used in the experiment, is dependent on several things. First, one needs to consider all the transmission losses through the optical elements, such as the microscope objective, dichroic filters and mirrors. Secondly, the coupling is strongly dependent on the overlap of the wavefront after the objective and the Gaussian mode of the optical fiber (see Chapter 4). The effective overlap is mainly

dependent of the quality of the optics involved, being the microscope objective and the fiber collimator.

A good estimate for the general ability of an objective to collect photons is the solid angles resulting from the NA that can be achieved by the respective objective. Since the photons during spontaneous emission are emitted isotropically (not the case if polarized photons are considered, see section 4.2), the solid angle determines the amount of photons which can be collected by a segment of a unit sphere. It is given by:

$$\Omega = \frac{4\pi \left(1 - cos(\theta)\right)}{2} \tag{3.3}$$

where θ is the half angle of the cone that can enter or exit the objective. The current objective was measured [19] to use an NA of 0.267 which corresponds to a collection of 1.63% of all emitted photons. The resulting collection efficiency η_{col} can be estimated in the following way:

$$\eta_{col} \approx \frac{P_{atom-photon}}{\frac{2}{3} \cdot \eta_{det} \cdot \eta_{pump}(T_{objective} \cdot T_{optics})}$$

$$= \frac{0.0022}{\frac{2}{3} \cdot 0.6 \cdot 0.8 \cdot 0.75} = 0.92\%$$

where $P_{atom-photon}$ is the success probability for atom-photon entanglement, η_{det} the photon detection efficiency, η_{pump} the efficiency for pumping in the excited state, $T_{objective}$ and T_{optics} the transmission through the objective and the remaining optics and the factor of $\frac{2}{3}$ since π polarized light is not used.

For the new objective we aim to use an NA of $0.35 - 0.50$. We may not be able to exploit the full NA of 0.5 due to several reasons. The first reason is, that the coupling efficiency of a collimated plane wave into a single-mode fiber has an upper limit, which is given by the overlap of a Gaussian beam with the top-hat shaped plane wave after the objective. This limit will be discussed in Chapter 4. Further, the collimator size used for coupling the light into the single mode fiber doesn't allow us to employ the full NA and the collimator lens can also introduce aberrations. However, since the objective is diffraction limited for the fluorescence wavelength we expect to have maximal overlap between the single-mode fiber and the collimated plane wave after the objective. In addition, the objective is specified for a transmission of $> 90\%$. Table 3.1 shows our estimated improvement for the photon collection efficiency for the new objective. The difference between collected photons and the collection efficiency comes from the overlap limit and the thermal movement of the atom in the trap and we expect a reduction of 35% (see Chapter 4). The result would be an overall improvement of the atom-atom entanglement rate by a factor of 6-29 compared to the current setup.

NA	collected photons	η_{col}	atom-photon ent.	atom-atom ent.
0.294	$4\pi \cdot 1.18\%$	0.92%	-	-
0.35	$4\pi \cdot 3.16\%$	2.43%	$\approx 2.5 \cdot \eta_{old}$ (expected)	$6 \cdot \eta_{old}$ (expected)
0.50	$4\pi \cdot 6.69\%$	4.96%	$\approx 5.4 \cdot \eta_{old}$ (expected)	$29 \cdot \Omega_{old}$ (expected)

Table 3.1.: Estimates for the factor of improvements of the photon collection efficiency in one trap and in both traps. Limiting factors are the efficiency for the coupling into the single mode fiber, the size of the collimator and aberrations induced by the collimator lens. In order to compare the two objectives, we assume the used NA for the current objective to be 10% as this was the optimal waist to aperture ratio found in Chapter 4.

Figure 3.4 shows the event rate for atom-atom entanglement including photon conversion to telecom band and the new objectives. It can be seen, that the new objective could more than compensate for the losses during the conversion to the telecom band and eventually yields an event rate of 0.5 events per minute at 20 km distance. This is calculated for an overall improvement by a factor of 10 compared to the current setup. However as discussed earlier, this is a conservative number and we hope to have a larger increase of photon collection efficiency. Nevertheless, already an event rate of 0.5 events per minute would allow us to generate and to characterize long-distance entanglement of atoms.
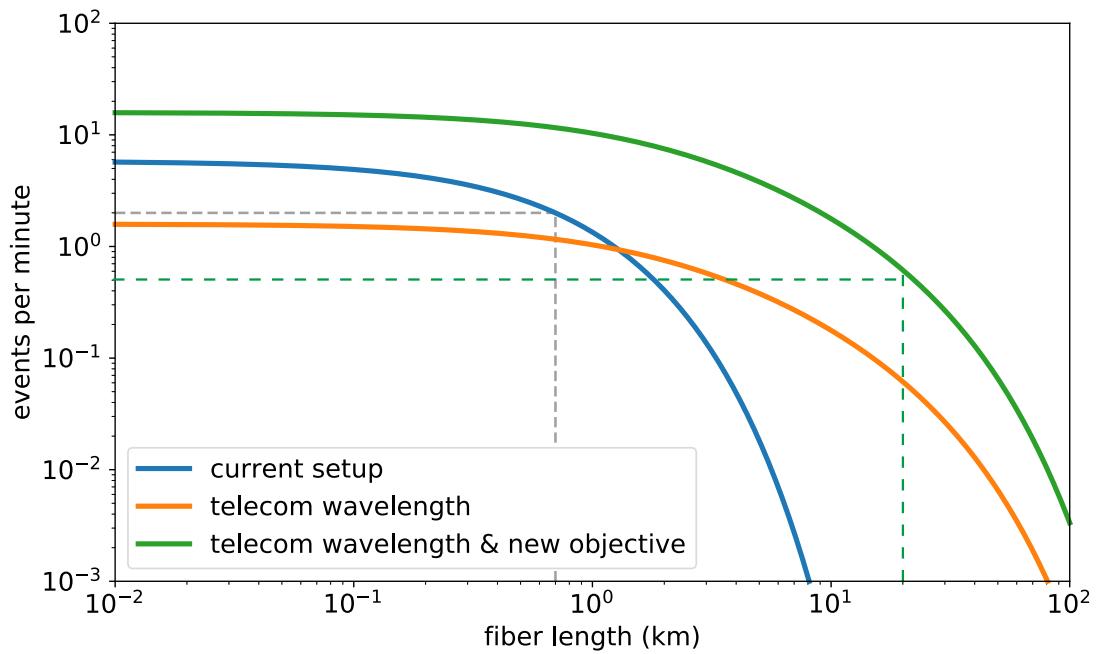
Figure 3.4.: Events per minute for wavelengths 780nm (old objective), 1522nm (old objective) and 1522nm including the new objectives. The gray dashed line shows the current event rate at a distance of 700m. The new objective could more than compensate for the conversion losses to the telecom yielding an estimate of 0.5 remote entanglement events per minute, for a fiber length of 20km shown by the green dashed line.

4. Photon coupling efficiency

In this chapter we investigate the coupling efficiency of photons which are emitted by the trapped atom into a single-mode fiber. The parameters which influence the coupling are the aperture size of the collecting objective, the beam size of the fiber collimator, as well as the position of the atom with respect to the focal plane and axis of the objective. In the optimal case, the atom position is longitudinal in the focal plane of the objective and transversal in the center of the round objective entrance pupil. However, due to residual thermal energy of the atom, its position will vary with respect to the optimal position. The impact of the atom position in the trap on the photon coupling efficiency will be investigated for longitudinal and transversal displacements separately. Further, a more precise approach will be conducted which includes the emission characteristics of dipole radiation. Eventually, longitudinal and transversal displacements are combined and the coupling efficiency will be calculated for different polarizations. The involved optics are assumed to be free of aberrations. This is very well fulfilled for the objective (Chapter 5.1) The not customized fiber collimator however is not optimized for our experiment and might induce aberrations.

4.1. Calculation of the fiber coupling efficiency for a point source

4.1.1. Optimal case

We first consider the simplest case, where the atom position in the trap is at the optical axis of the objective and in the focal plane, the photon emission of the atom can be approximated as a point source of 780nm light which is converted into a collimated plane wave by the objective (see figure 4.1). In a first approximation, we assume the intensity distribution of the collimated beam after the objective to be uniform over the objective pupil. The mode which gets coupled into the fiber is a collimated Gaussian (TEM_{00}). There we do not consider polarization emission characteristics of the atomic dipole.

The resulting coupling efficiency of the plane wave emitted by the atom and the well-defined spatial eigenmode (TEM_{00}) of the optical fiber, can be expressed in cylinder coordinates as:
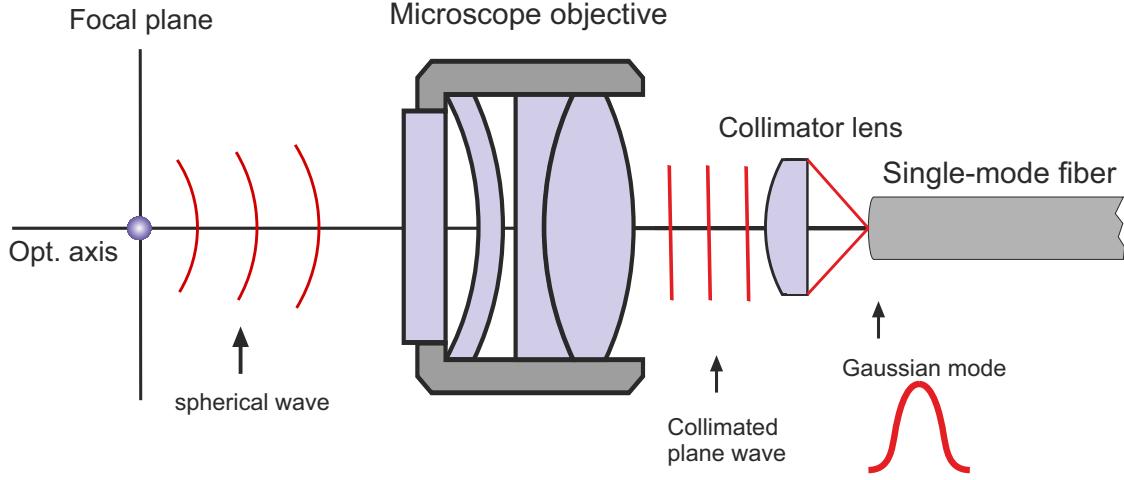
Figure 4.1.: The atom is at the axis of the objective and in the focal plane. The emission of the atom is approximated as a point source. The spherical waves get then converted by the objective into a collimated plane wave and coupled into a single-mode fiber.

$$O^2\left(\frac{w_0}{R_0}\right) = |\int_0^{2\pi} d\varphi \int_0^\infty E_{gauss}^* E_{atom} r \cdot dr|^2 \tag{4.1}$$

$$E_{gauss} = \frac{1}{\sqrt{\frac{\pi}{2}}w_0} e^{-\frac{r^2}{w_0^2}}$$

$$E_{atom} = \frac{1}{\sqrt{\pi}R_0}\Theta(R_0 - r)$$

where E_{gauss} denotes the Gaussian eigenmode of the fiber after collimation to a beam waist w_0 and E_{atom} the normalized top-hat shaped electric field emitted by the atom and collected by the objective with a pupil radius R_0.

Figure 4.2 shows the resulting normalized coupling efficiency $O^2(\frac{w_0}{R_0})$ as a function of the ratio of the radius of the objective pupil and the waist of the fluorescence collection. It can be seen, that the maximum achievable coupling efficiency is 81.45% which gives the upper limit for in other respects perfect coupling conditions regarding the position and alignment of the atom to the objective. The according optimal waist to objective pupil ratio is 89.3%. One way to overcome this limit would be to adapt the collimation optics in such a way, that the Gaussian eigenmode of the fiber is transformed into a top-hat mode, i.e. a uniform intensity distribution over the size of the objective pupil. While being difficult to implement, this would be a possible upgrade for
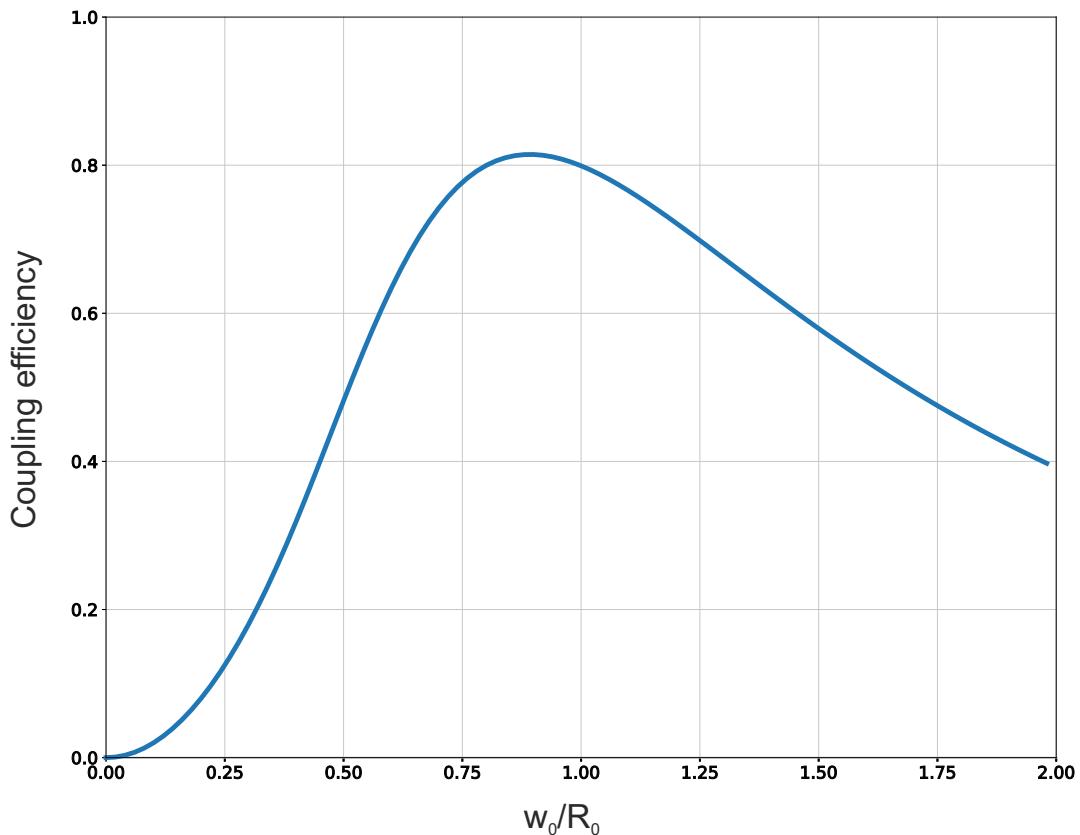
Figure 4.2.: Coupling efficiency of a Gaussian beam with top hat shaped aperture of the objective as a function of the waist of the beam and the objective pupil radius. The maximal coupling efficiency is 81.45% with a optimal waist to objective pupil ratio of 89.3%.

future iterations of the setup in order to exceed the currently achievable overlap between the mode of the collected light and the mode of the optical fiber.

4.1.2. Thermal velocity distribution of the atom in the trap

The case discussed in 4.1.1 considers the case of the atom exactly at the optical axis and in the focal plane of the objective. However, this is not the case in the real experiment. The cooling of the atom has low but however not vanishing temperature limits and thus the atom has residual thermal energy. According to measurements, the temperature of the atom is $45\mu K$. At these low temperatures and thereby low thermal energy of the atom the dipole trapping potential of 3.2 mK can well be approximated by a three-dimensional harmonic oscillator. The spatial probability distribution of the atom in radial and longitudinal direction is in thermal equilibrium a Gaussian shape given by:

$$P_{th}(z) = \sqrt{\frac{m\Omega_z^2}{2\pi k_B T}} e^{-\frac{z^2}{\frac{2k_B T}{m\Omega_z^2}}} \tag{4.2}$$

$$P_{th}(r) = \sqrt{\frac{m\Omega_r^2}{2\pi k_B T}} e^{-\frac{r^2}{\frac{2k_B T}{m\Omega_r^2}}} \tag{4.3}$$

where m is the mass of the atom, k_B the Boltzmann constant z the longitudinal position, r the radial position, T the temperature and $\Omega_{r,z}$ the respective trap frequency. The trap frequency is basically the oscillation rate of the atoms in the trap and is usually computed via harmonic approximation in the trap center. Due to symmetry properties of the trap we distinguish between radial (x- and y-direction) and longitudinal (z-direction) trap frequencies. They are given by:

$$\Omega_r = \sqrt{\frac{4U_0}{mw_0^2}} \tag{4.4}$$

$$\Omega_z = \sqrt{\frac{2U_0}{mz_R^2}} \tag{4.5}$$

In our experiment the trap depth is $U_0 = 3.2\text{mK} \cdot k_B$, the temperature of the atom $T = 45\mu K$, the waist of the dipole trap $w_0 = 1.92\mu m$ which corresponds to a Rayleigh length of $z_R = 13.6\mu m$. The standard deviations of the spatial atom position has the following form, again in radial and longitudinal direction:

$$\sigma_r = \sqrt{\frac{4-\pi}{2}} \cdot \sigma_x = \sqrt{\frac{4-\pi}{2}} \cdot \sqrt{\frac{k_B T}{4U_0}} w_0 = 74.51\text{nm} \tag{4.6}$$
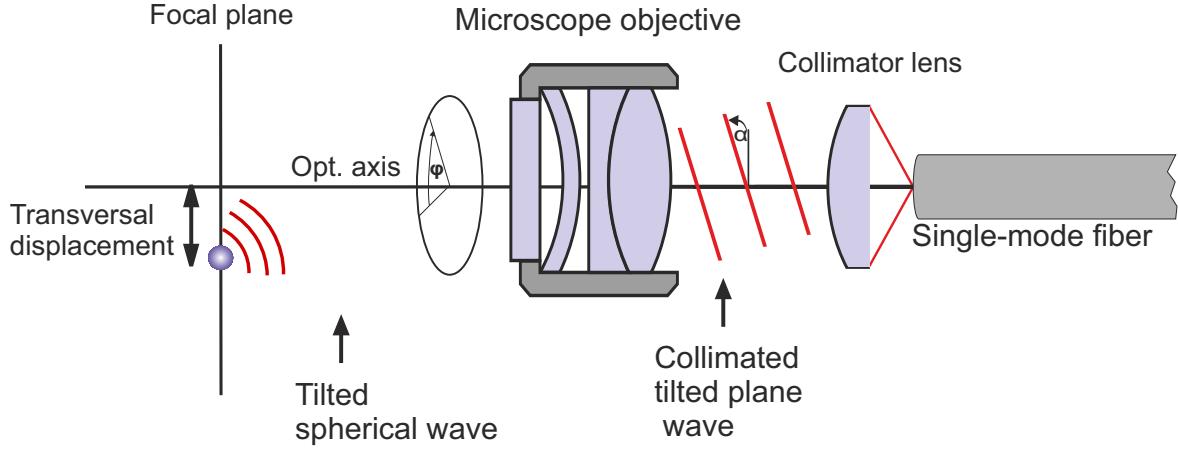
Figure 4.3.: The atom is displaced from the optical axis due to its thermal energy. For radial displacement this leads to a transversal tilt of the emitted plane which reduces the coupling efficiency.

$$\sigma_z = \sqrt{\frac{k_B T}{2 U_0}} z_R = 1.13 \mu m \tag{4.7}$$

The following part will investigate the impact of transversal displacement of the atom relative to the optical axis. The photons emitted from the atom in the focus can be approximated as plane waves at the surface of the objective, i.e. there is no tilt between the plane waves and the objective. However, if there is a displacement of the atom due to its thermal energy, the result is a different photon emission point of the atom. This leads to a tilt in the plane waves relative to the objective axis (see figure 4.3)

The phase profile of the tilted plane wave has the following form:

$$E_{atom} = \frac{1}{\sqrt{\pi R_0}} \Theta \left(R_0 - r \right) e^{-i \Psi(r, \varphi)} \tag{4.8}$$

where Ψ is the phase shift induced from the tilt. It is given by:

$$\Psi(r, \varphi) = k_t \cdot r \cdot cos\varphi \tag{4.9}$$

with $k_t = \frac{2\pi}{\lambda} \cdot sin(\alpha)$ being the transversal k-vector, α the angle between the plane wave and the optical axis surface (see figure 4.3) and $r \cdot cos(\varphi)$ describing the plane wave in polar coordinates.

Plot a) in figure 4.4 shows the overlap of the TEM_{00} Gaussian eigenmode of the optical fiber with the plane wave emitted by the atom. The x-axis shows the ratio of Gaussian waist to objective entrance pupil. The y-axis shows the corresponding fraction of the plane wave that is coupled into the fiber, i.e. the coupling efficiency. As already discussed in 4.1.1 the limit of the coupling probability between a plane wave and a Gaussian beam is 81.45% with $\frac{w_0}{R_0} = 89.3\%$. Whenever the atom is displaced due to, e.g., thermal motion inside the trap, the emitted plane wave gets a phase shift as given in equation 4.8. The phase shift reduces the coupling efficiency and also shifts the optimal $\frac{w_0}{R_0}$-ratio. In plot a) in figure 4.4 we plotted the coupling efficiencies for several atom displacements in transverse direction. It can be seen that there is a reduction in coupling efficiency as a function of displacements. An atom position of $\sigma_r (= 74.51\text{nm})$ radially away from the optical axis only reduces the coupling efficiency by 5% as compared to a displacement of $4 \cdot \sigma_r$ which already yields a reduction of 20%. For a good estimation for the coupling efficiency it is necessary to account for the probability that an atom is actually displaced to a certain position. Therefore, we integrate over the individual coupling efficiency for different displacements by weighting with the 2-D radial position probability density function of the thermal distribution function of the atom in the trap (see equation 4.2). This is done by expressing the plane wave and the thermal distribution as a function of displacement Δr. The resulting integral has the following form:

$$O_{weighted}\left(\frac{w_0}{R_0}\right) = |\int_0^{5 \cdot \sigma_r} d\Delta r \int_0^{2\pi} d\varphi \int_0^\infty dr E_{gauss}^* \left(r, w_0\right) E_{atom}\left(r, \Delta r, \varphi\right) P_{th}\left(\Delta r\right) \cdot r^2|^2$$

(4.10)

The lower plot in figure 4.4 shows the resulting collection efficiency which is weighted with the probability density function for the position of the atom in the trap in radial direction. The maximal achievable overlap is 75.13% for an optimal ratio of $\frac{w_0}{R_0} = 88.05\%$. The graph also depicts the actual waist used in the new microscope objective setup, which is slightly smaller than the optimal one and has a $\frac{w_0}{R_0}$-ratio of 72%. The reasons for using this particular waist are discussed in more detail in Chapter 5.1.1.1. With this approach we eventually obtain an estimate for the maximal radial coupling efficiency of 70.05% with the new microscope objective setup.

4.1.3. Longitudinal atom displacement

Besides radial displacement, the atom has an additional degree of freedom in the trap, which is the movement in z-direction, i.e., moving outside of the focal plane of the microscope objective. In that case, the wavefront of the atom after the objective can be described as a spherical wave with curvature R_c. The curvature and thereby the resulting phase shift is dependent on the displacement in z-direction (see figure 4.5). The electric field emitted by the atom after the objective has the following form:
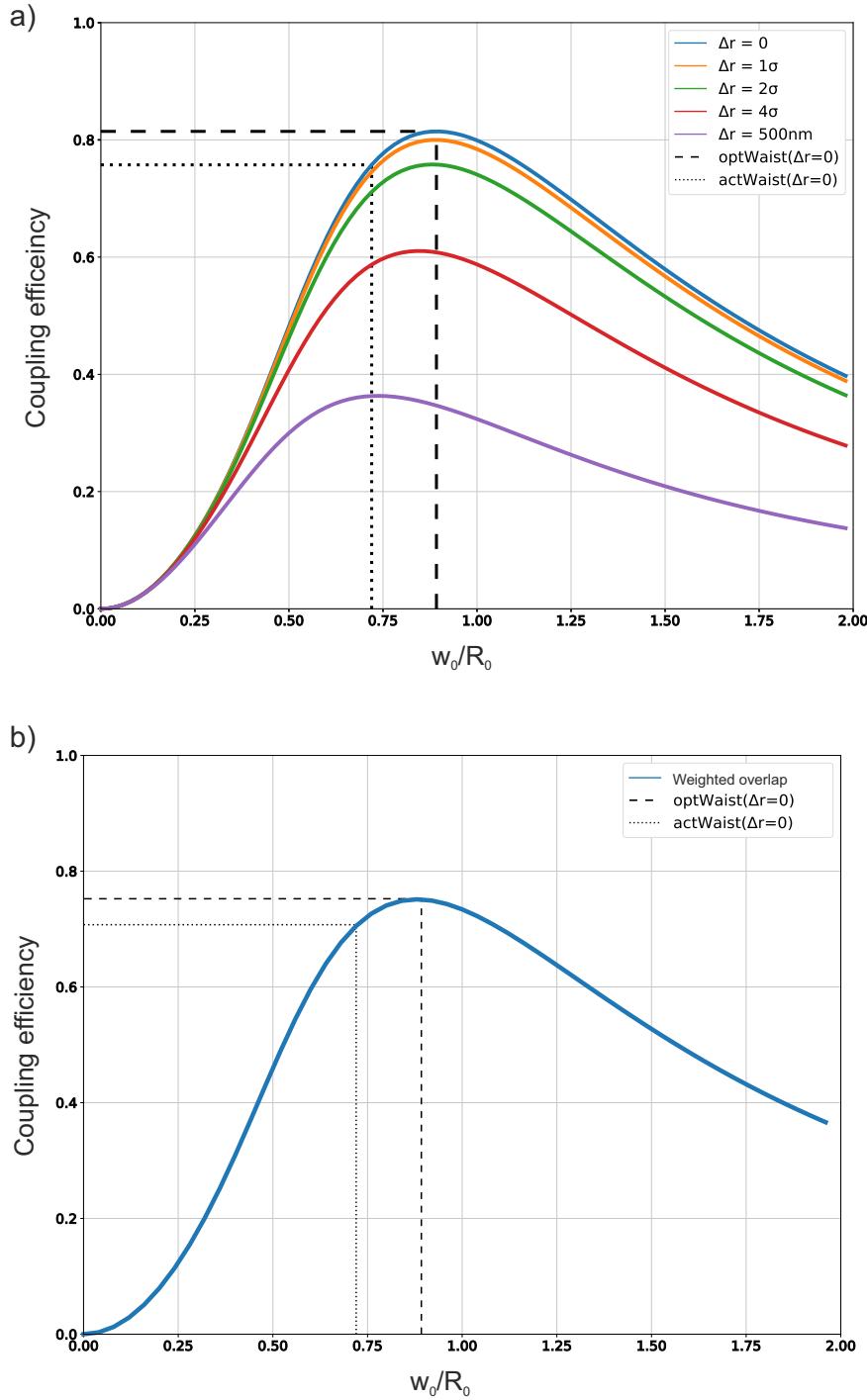
Figure 4.4.: **(a)** Overlap integral of the TEM_{00} eigenmode of the optical fiber with the plane wave emitted by the atom as a function of the Gaussian waist w_0 and the entrance pupil radius of the objective R_0. The chosen displacements are given with respect to the calculated thermal distribution with $\sigma_r = 75$ nm. Further, the optimal $\frac{w_0}{R_0}$ value and the corresponding coupling efficiency is depicted. **(b)** Overlap integral is weighted by the probability density function for the atom position in z-direction. The resulting maximum overlap is 73.23% with $\frac{w_0}{R_0} = 72\%$.
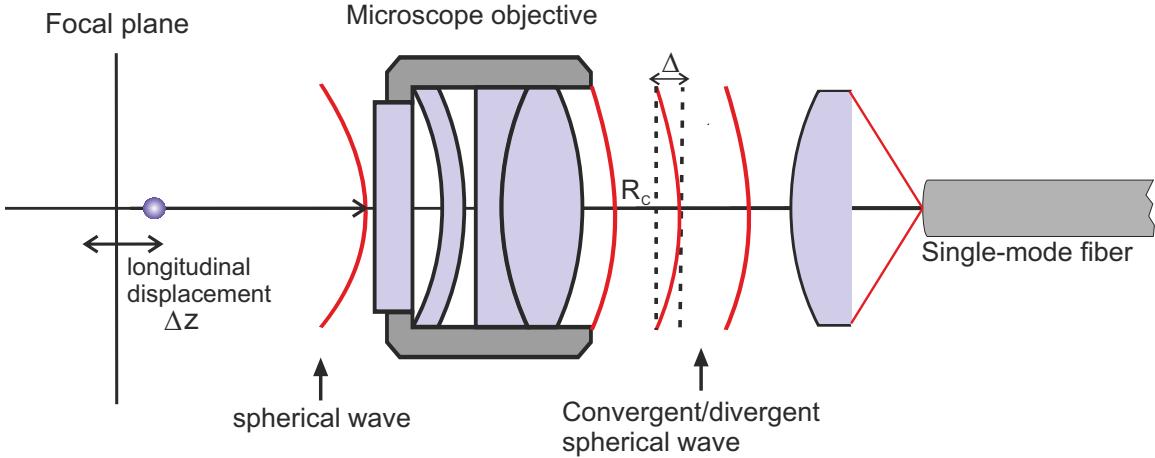
Figure 4.5.: The atom is displaced from the focal plane due to its thermal energy. For longitudinal displacement this leads to a change of curvature of the spherical wave after the objective which reduces the coupling efficiency.

$$E_{atom} = \frac{1}{\sqrt{\pi}R_0}\Theta\left(R_0 - r\right) \cdot e^{-i\Psi(r,R_c)} \tag{4.11}$$

where Ψ is the phase shift induced by the displacement in z-direction. It is dependent on the curvature of the spherical wave R_c, which itself is dependent on displacement Δz in the focal-plane and the focal length f.

$$\Psi(r, R_c) = 2\pi \cdot \frac{\Delta}{\lambda} = \frac{2\pi}{\lambda} \cdot R_c \left(\sqrt{1 + \frac{r^2}{R_c}} - 1 \right) \tag{4.12}$$

$$R_c = \frac{(f + \Delta z) \cdot f}{\Delta z} \tag{4.13}$$

R_c results from the lens formula:

$$\frac{1}{f} = \frac{1}{f + \Delta z} + \frac{1}{R_c}$$

Figure 4.6 shows the resulting coupling efficiency for several longitudinal displacements as a function of $\frac{w_0}{R_0}$. Clearly the coupling efficiency shows similar behavior as for transverse displacement, i.e. an optimal $\frac{w_0}{R_0}$-ratio of 88.05% with an overlap of 81.45% and decreasing overlaps

for larger displacements. However, a displacement of σ_z by a factor of 15 larger than σ_r only reduces the coupling to 73%. This means, that in terms of absolute distances, a longitudinal atom position shift is less crucial compared to a transverse drift. The reason for that is the larger depth of focus in longitudinal direction than the field of view in transversal direction. In longitudinal direction from the focus, the beam size is increased by $\sqrt{2}$ after the Rayleigh length, which is $z_R = 13.6\,\mu m$. In transverse direction, the beam has only a waist of 800 nm and thereby changes faster with distance. From that follows, when considering the same absolute displacement, the atom plane remains in sharper focus in longitudinal - than in transverse direction. However, due to similar reasons, the longitudinal extension of the thermal distribution is larger than the radial.

In order to include the probability for the atom being displaced from the focal point, we again weight the overlap integrals for different displacements with the 1-D probability density function for the thermal atom distribution (equation 4.2) in z-direction. A similar calculation as in equation 4.10, now integrating over Δz yields an averaged overlap integral which is depicted in figure 4.6. With an actual $\frac{w_0}{R_0}$-ratio of 72% this yields an on average longitudinal overlap of 73.23%.

Conclusion

From the previously described approach to determine the coupling efficiency of the photon emission of the atom in the trap we conclude two things. First, no matter how good the quality of our optics is, the coupling efficiency of the photons into the single mode fiber will always be limited to the maximal threshold for the overlap of a Gaussian beam and a top-hat function of 81%. Thermal motion of the atom in the trap further reduces this value. In order to overcome this limit it would be necessary to convert the Gaussian beam into a flat top-hat profile, i.e. a uniform intensity distribution with the radius of the objective aperture. However, at the time this thesis was written, no industrial available converter was found that could be used for our beam size and wavelength.The second thing we conclude is on the sensitivity for the alignment precision when overlapping the dipole trap and the fluorescence collection. As shown in the figure 4.4 and 4.6, errors in the positioning of the atom become critical above a displacement of ~ 150 nm in radial direction and $\sim 1\mu m$ in z-direction. Hence the alignment precision has to be more thoroughly conducted in radial direction and must not exceed an error of ~ 150 nm. The alignment procedure and the effects that we have to take into account for reaching this precision will be described in Chapter 5.
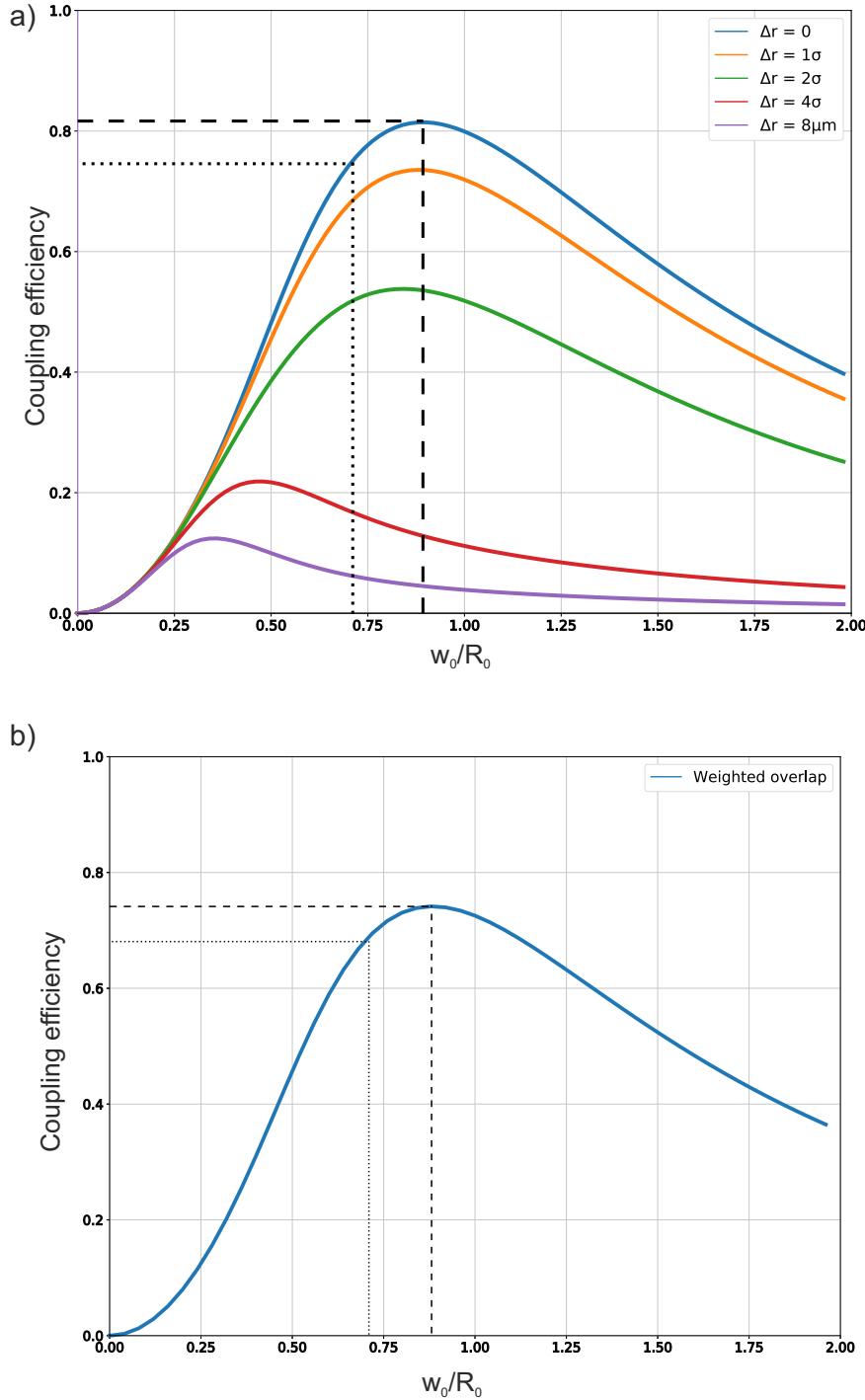
Figure 4.6.: **(a)** Overlap integral of the TEM_{00} eigenmode of the optical fiber with the plane wave emitted by the atom as a function of the Gaussian waist w_0 and the entrance pupil radius of the objective R_0. The chosen displacements are given with respect to the calculated thermal distribution with $\sigma_z = 1.13 \ \mu m$. Further, the optimal $\frac{w_0}{R_0}$ value and the corresponding coupling efficiency is depicted. **(b)** Overlap integral is weighted by the probability density function for the atom position in z-direction. The resulting maximum overlap is 73.23% with $\frac{w_0}{R_0} = 72\%$.

4.2. Dipole nature of the atomic emission

The previously described ansatz is a simple and intuitive approach to determine the photon coupling efficiency into a single-mode fiber. However, the main disadvantage is that longitudinal and transverse atom displacement effects have to be considered separately. Further, especially for our experiment, it is necessary to consider polarized photons as this is the property which contains the information of the photon we are interested in. Thus, it is necessary to include the dipole emission characteristics of the atom. This has the consequence, that the distribution of the photon emission can no longer be assumed to be spherical, but is dependent on the angle and the polarization of the emitted photons.

4.2.1. Analytical expressions for the dipole emission characteristics

The emission of an atomic dipole can be described by a superposition of the electric fields E_x, E_y and E_z which are oriented along the unit vectors $\boldsymbol{e_x}$, $\boldsymbol{e_y}$ and $\boldsymbol{e_z}$ respectively (see figure 4.7). The emission modes of the three orthogonal linear atomic dipoles oscillating along x (H-polarization), y (V-polarization) and z (π-polarization), are given by [26, 17]:

$$\boldsymbol{E_a^H} = \frac{e^{ikr}}{r} E_a^H \left[(\boldsymbol{e_r} \times \boldsymbol{e_x}) \times \boldsymbol{e_r} \right] \tag{4.14}$$

$$\boldsymbol{E_a^V} = \frac{e^{ikr}}{r} E_a^V \left[(\boldsymbol{e_r} \times \boldsymbol{e_y}) \times \boldsymbol{e_r} \right]$$

$$\boldsymbol{E_a^{\pi}} = \frac{e^{ikr}}{r} E_a^{\pi} \left[(\boldsymbol{e_r} \times \boldsymbol{e_z}) \times \boldsymbol{e_r} \right]$$

where E_a^H, E_a^V and E_a^{π} are the normalization factors and $\boldsymbol{e_r}$ the unit vector pointing along the radial direction in the spherical coordinate system defined in figure 4.7. Here, z defines the optical axis of the objective and x and y the plane perpendicular to the optical axis. θ is the polar angle in spherical coordinates and φ the azimuth angle (see figure 4.7). We use the following definition for the radial unit vector in spherical coordinates:

$$\boldsymbol{e_r} = \begin{pmatrix} sin\theta \cdot cos\varphi \\ sin\theta \cdot sin\varphi \\ cos\theta \end{pmatrix}$$
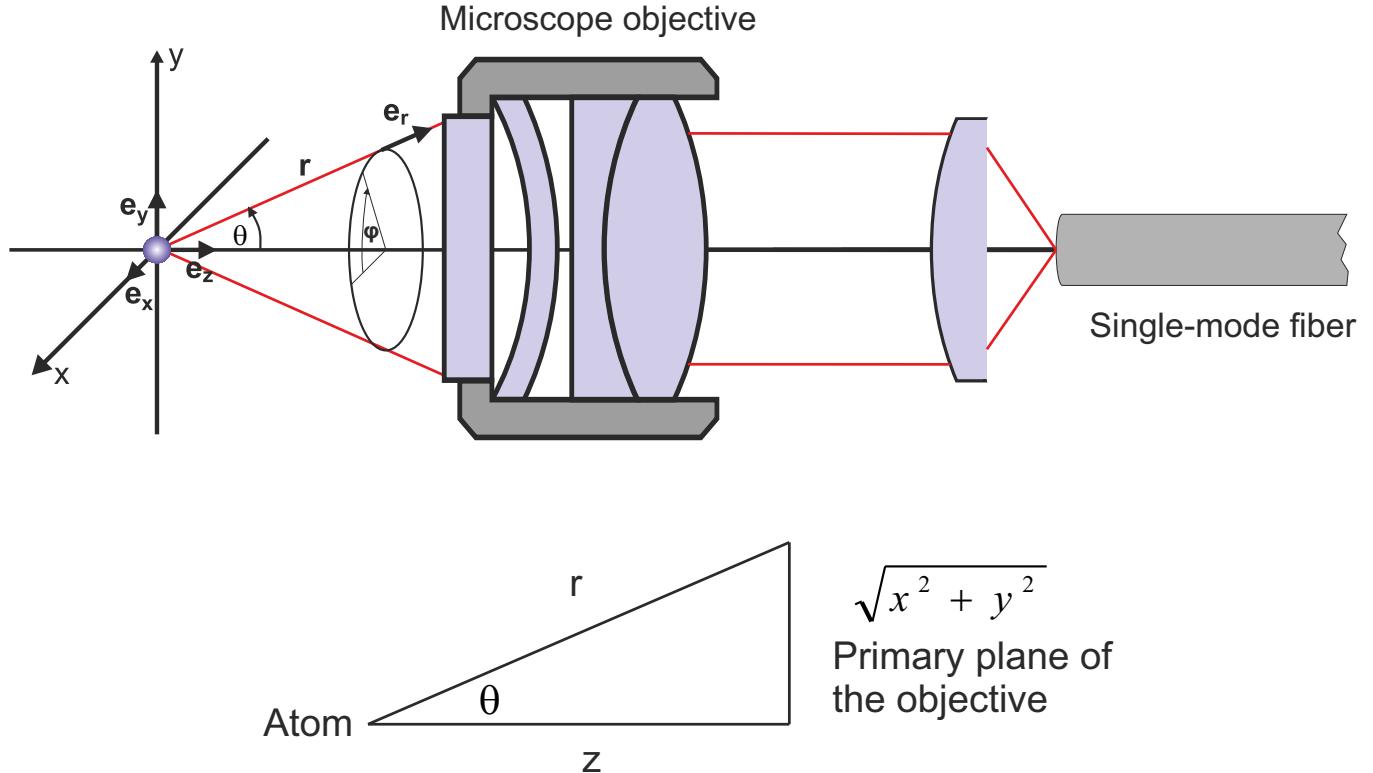
Figure 4.7.: The fluorescence light follows the classical dipole radiation from an atomic dipole arranged along the unit vectors e_x, e_y and e_z. The x and y plane define the plane perpendicular to the optical axis of the objective.[26].

Normalization constants

In a later part of the investigation we want to allow displacements of the atom in x, y and z-direction which is more comfortable to do in Cartesian coordinates. Therefore, we like to formulate our description of the atomic dipole emission in Cartesian coordinates. To arrive at a normalized electric field distribution in the primary plane of the objective, one has to consider two things. First, we have to normalize the cross product and thereby the electric field distribution in x, y and z-direction.

$$\left| (e_r \times e_x) \times e_r \right|^2 = 1 - sin^2\theta \cdot cos^2\varphi = \frac{y^2 + z^2}{x^2 + y^2 + z^2} \tag{4.15}$$

$$\left| (e_r \times e_y) \times e_r \right|^2 = cos^2\theta + cos^2\varphi \cdot sin^2\theta = \frac{z^2 + x^2}{x^2 + y^2 + z^2}$$
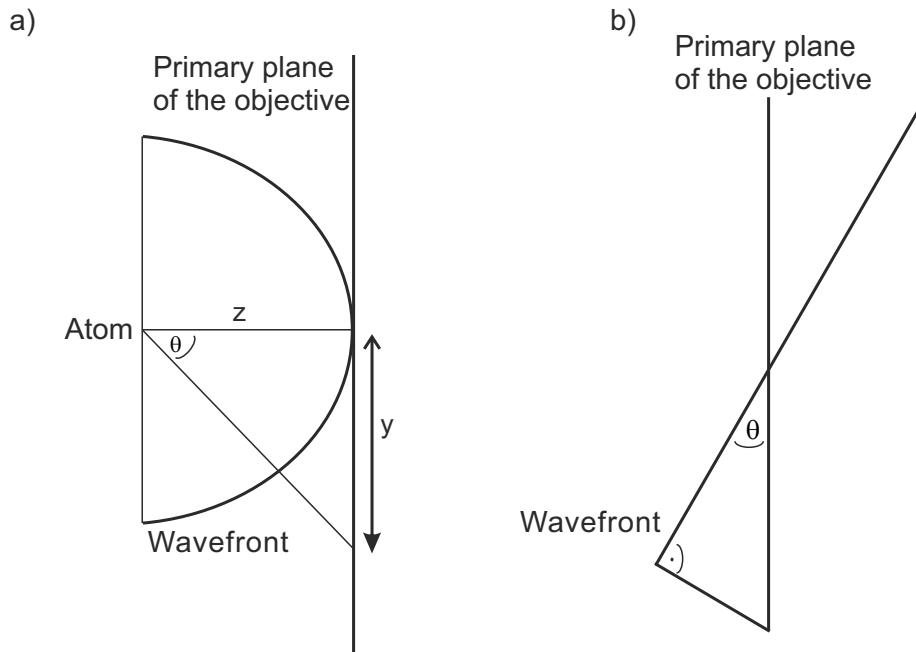
Figure 4.8.: (a) The spherical projection describes the conversion from an angle element of a sphere onto an surface element in a plane. (b) Derivation of the scaling factor by considering an infinitesimal small part of the intersection, where the spherical wave can be approximated plane.

$$\left|(\boldsymbol{e_r} \times \boldsymbol{e_z}) \times \boldsymbol{e_r}\right|^2 = sin^2\theta = \frac{x^2 + y^2}{x^2 + y^2 + z^2}$$

Furthermore, when transforming the spherical description of the dipole emission into Cartesian coordinates, we have to keep in mind the projection factor. The projection describes the mapping of a sphere onto a plane and hence gives a scaling factor for a change in angle to a corresponding surface element.The basic idea of the transformation of an angle element onto the plane is depicted in figure 4.8 (a). For calculating the scaling factor, we consider infinitesimal small regions of the intersection between primary plane of the objective and wavefront. In that case, the relationship between the length of the wavefront and the corresponding projection onto the primary plane of the objective is given by $1/cos\,(\theta)$, i.e. that the length of the projection in the plane is larger by $cos\,(\theta)$ compared to the length of the corresponding angle element of the sphere (see 4.8 (b). This scaling factor is independent of φ and r since the previously stated argument is valid for any arbitrary intersection of the wavefront with the primary plane of the objective.

Combining the equations for the normalization of the scaling factor and 4.15 with eqn. 4.14 gives the normalized description of the atomic dipole emission (for more detail derivation see Appendix A):

$$\boldsymbol{E_a^H}(x,y,z) = \frac{e^{ik\sqrt{x^2+y^2+z^2}}\sqrt{z}}{(x^2+y^2+z^2)^{\frac{5}{4}}\sqrt{y^2+z^2}} \cdot \begin{pmatrix} \sqrt{\frac{3}{4\pi}}(y^2+z^2) \\ -\sqrt{\frac{3}{\pi}}\cdot y \cdot x \\ -\sqrt{\frac{3}{\pi}}\cdot z \cdot x \end{pmatrix} \qquad (4.16)$$

$$\boldsymbol{E_a^V}(x,y,z) = \frac{e^{ik\sqrt{x^2+y^2+z^2}}\sqrt{z}}{(x^2+y^2+z^2)^{\frac{5}{4}}\sqrt{x^2+z^2}} \cdot \begin{pmatrix} -\sqrt{\frac{3}{\pi}}\cdot y \cdot z \\ \sqrt{\frac{3}{4\pi}}(x^2+z^2) \\ -\sqrt{\frac{3}{\pi}}\cdot z \cdot y \end{pmatrix} \qquad (4.17)$$

$$\boldsymbol{E_a^\pi}(x,y,z) = \frac{e^{ik\sqrt{x^2+y^2+z^2}}\cdot\sqrt{z}}{(x^2+y^2+z^2)^{\frac{5}{4}}\cdot\sqrt{x^2+y^2}} \cdot \begin{pmatrix} -\sqrt{\frac{3}{\pi}}\cdot z \cdot x \\ -\sqrt{\frac{3}{\pi}}\cdot z \cdot y \\ \sqrt{\frac{3}{4\pi}}(x^2+y^2) \end{pmatrix} \qquad (4.18)$$

These formulas for the dipole emission characteristics are a normalized representation for the polarization dependent emission pattern of the atom in our experiment.

4.2.2. Photon collection of the objective

As described previously, the coupling of photons into the single mode fiber is determined by the amount of photons which can be collected by objective and the subsequent coupling efficiency into the single mode fiber of the collected light. The following part will discuss and calculate the amount of photons that can be collected by the objective considering the NA of the objective and the emission pattern.

The time-averaged power radiated per unit solid angle by the oscillating dipole with a specific polarization is given by the Poynting vector projected in radial direction. As derived in [17], it is calculated as:

$$\frac{dP}{d\Omega} \sim \left|(\boldsymbol{e_r}\times\boldsymbol{e_p})\times\boldsymbol{e_r}\right|^2 \qquad (4.19)$$

where e_p denotes the unit vector for the respective oscillating dipole moment $\boldsymbol{e_x}$, $\boldsymbol{e_y}$ and $\boldsymbol{e_z}$. As an exemplary case we will consider in the following the atom to be oscillating in $\boldsymbol{e_x}$ direction (i.e. H-polarization). Then formula 4.19 yields:

$$\frac{dP}{d\Omega} \sim \left|(\boldsymbol{e_r}\times\boldsymbol{e_p})\times\boldsymbol{e_r}\right|^2 = cos^2\theta + sin^2\theta \cdot sin^2\varphi \qquad (4.20)$$

The respective normalized fraction of H-polarized photons that are collected by the objective with an NA of 0.5 and hence an opening angle $\theta = 30°(=\frac{\pi}{6})$ is then given by:

$$N_{Photon}(NA = 0.5) = \frac{\int_0^{2\pi} d\varphi \int_0^{\frac{\pi}{6}} (cos^2\theta + sin^2\theta \cdot sin^2\varphi) \cdot sin\theta \cdot d\theta d\varphi}{\int_0^{2\pi} d\varphi \int_0^{\pi} (cos^2\theta + sin^2\theta \cdot sin^2\varphi) \cdot sin\theta \cdot d\theta d\varphi} = 0.094 \quad (4.21)$$

that means, that 9.4% of all emitted H-polarized photons of the atom can be collected by the objective. Comparing the amount of photons collected per unit solid angle when considering unpolarized photons with a spherical emission pattern as estimated in section 3.3 yields $N_{photonUnpolarized}(NA = 0.5) = 6.7\%$. The rise in collected photons comes from the predominant emission of H-polarized photons into the direction of the quantization axis, which is in the experiment defined by the objective. Hence the polarization dependent intensity on the primary plane of the objective is not uniform but has a shape across the objective which is similar to a Gaussian. Figure 4.9 a) shows the intensity across the plane of the objective pupil in x- and y-direction for the x-component of E_H, which corresponds to the H-polarized photons from the dipole oscillating in x. The x and y position is given in pupils coordinates for an NA of 0.5. The green line shows a Gaussian with the same parameters in both plots. Clearly, the shape is different in x and y-direction, with a larger extension in y-direction as this can also be seen in the 2D plot in (b). The asymmetry of the intensity distribution stems again from the angle dependence of the atomic dipole emission for H-polarized photons. When the dipole is oscillating in x-direction, the emission in x goes to zero for $\theta \to 90$, whereas the emission in y-direction is only reduced by the spherical projection factor of the emission on the 2D primary plane of the objective. Hence the reduction in intensity is faster in x as in y-direction.

The behavior for V-polarized photons is completely similar to the H-polarized case, with only being rotated by $90°$, i.e. the ellipse has its larger extension in x-direction than in y-direction. The absolute numbers for the collection and intensity remain the same.

4.2.3. Calculation of the collection efficiency for an atomic dipole

We consider the simplest case, where the atom position in the trap is at the axis of the objective and in the focal plane. By the vector description of the atomic emission including the normalized dipole emission characteristics we are able to evaluate the expected collection efficiency for the microscope objective. In that case, the resulting collection efficiency for H-polarized emission of the atom can be expressed by:

$$O^2 \left(\frac{w_0}{R_0}\right) = |\int_{-\sqrt{R_0-y^2}}^{\sqrt{R_0-y^2}} \int_{-R_0}^{R_0} E_{gauss}^* E_{atom} dx dy|^2 \quad (4.22)$$
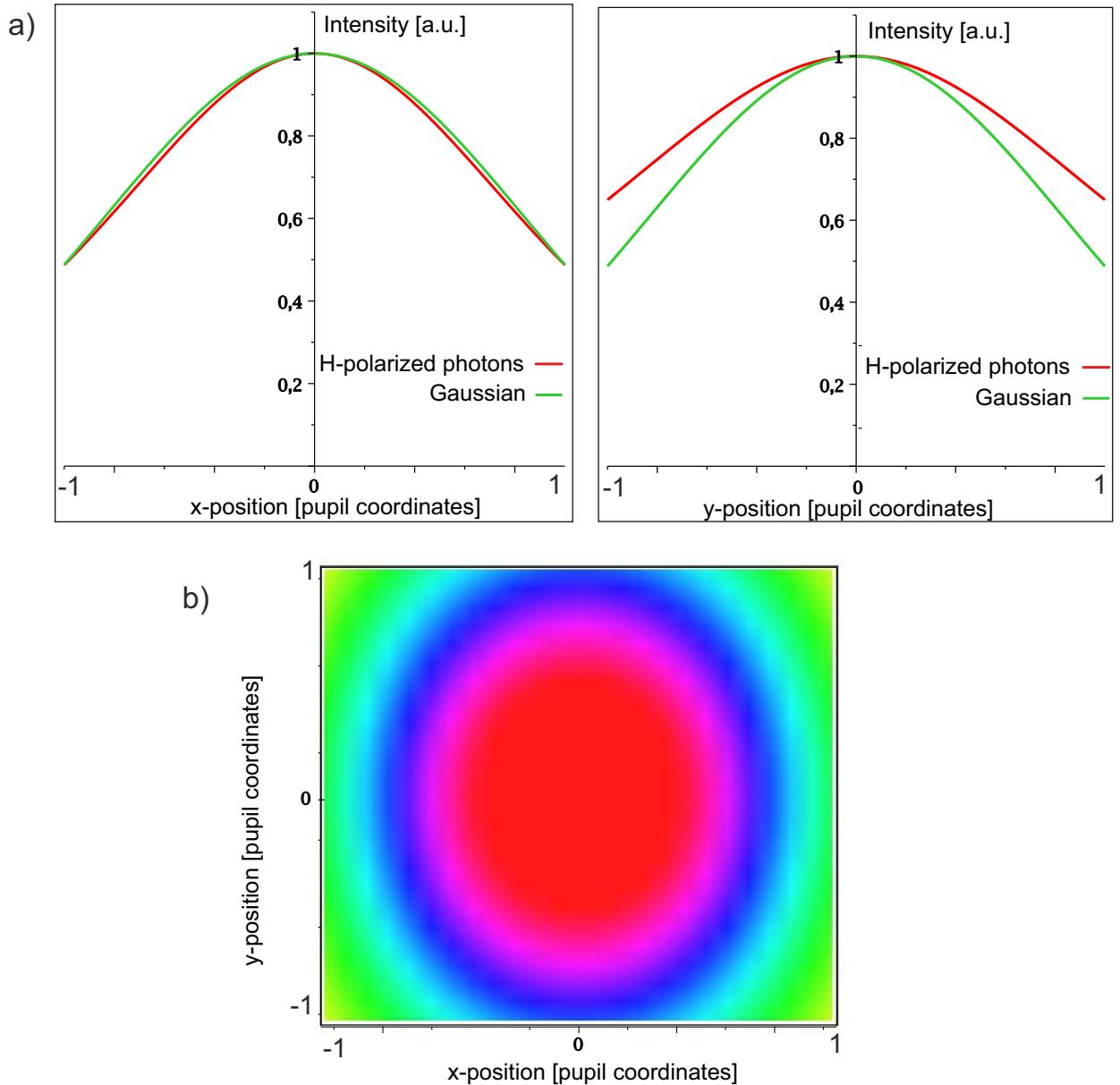
Figure 4.9.: a) Cross section of the H-polarized photon intensity on the primary plane of the objective in x-y direction. The red line depicts the photon intensity and the green line a Gaussian fit with the same parameters for both plots. b) 2D plot of the photon intensity distribution on the primary plane of the objective. The shape for H-polarized photons is an ellipse with a larger extension in y direction.

$$E_{gauss} = \frac{1}{\sqrt{\frac{\pi}{2}}w_0} e^{-\frac{r^2}{w_0^2}} e^{\left(-ikf\left(\sqrt{1+\frac{x^2+y^2}{f^2}}-1\right)\right)}$$

$$E_{atom} = e^{ik\sqrt{x^2+y^2+f^2}} \cdot \sqrt{\frac{3}{4\pi}} \cdot \frac{\sqrt{(y^2+f^2)} \cdot \sqrt{f}}{(x^2+y^2+f^2)^{\frac{5}{4}}}$$

where E_{gauss} is the Gaussian eigenmode of the fiber after passing the objective and E_{atom} the atomic dipole emission at the front side of the objective (i.e. $z = f$). The result is the fraction of the H-polarized photons that are coupled into the fiber as H-polarized photons which is shown in figure 4.10. The resulting maximal collection efficiency is 8.07% with an optimal waist to objective pupil ratio of 85.44%. This number for the collection efficiency is the maximum achievable value, considering no further losses, such as quality of the fiber collimator, transmission losses in the optics or the thermal distribution of the atom in the trap. The coupling efficiency for the case of atomic dipole emission characteristics is 85%. This is about 6% more than the previously considered case for unpolarized photons and hence a spherical emission pattern. This is a consequence of the less flat like shape of the emission for H-polarized photons and thereby larger overlap with the Gaussian TEM_{00} eigenmode of the optical fiber.

Due to symmetry reasons, we will get the same result for the collection efficiency for V-polarized photons. When considering the atom at rest in the origin, i.e., to have no thermal distribution in the trap, the collection efficiency for π-polarized photons will always be zero. This is due to the fact that the emission pattern of π-polarized light is antisymmetric with respect to quantization axis and hence the objective axis. Evaluating the integral in equation 4.22 yields the product of an antisymmetric function (π-emission) and a symmetric function (Gaussian eigenmode) integrated over the spherical objective aperture which is always zero, independent of the collection angle of the objective.

Conclusion

Describing the atomic emission including the normalized dipole emission characteristics allows us to precisely quantify the photon collection rate of the objective and the coupling efficiency into the single mode fiber. Hence we are able to give an absolute number for the photon collection efficiency reachable by the new objective. Assuming to have no other losses due to for example bad fiber collimator quality or other transmission losses, we get a maximal possible photon collection efficiency of 8.07%. Table 4.1 compares the results for the two approaches for the atomic emission description. It clearly shows that the more realistic case, which considers polarized photons, yields a higher photon collection efficiency for two reasons. The first one is the predominant emission of H- and V-polarized photons into the direction of the objective and hence results in a larger photon collection rate. The second reason is the larger coupling efficiency into the single mode fiber, which is due to the shape of the intensity distribution. The intensity distribution of polarized photons has a larger overlap with the Gaussian eigenmode of the single-mode fiber compared to the top-hat intensity distribution of unpolarized photons.
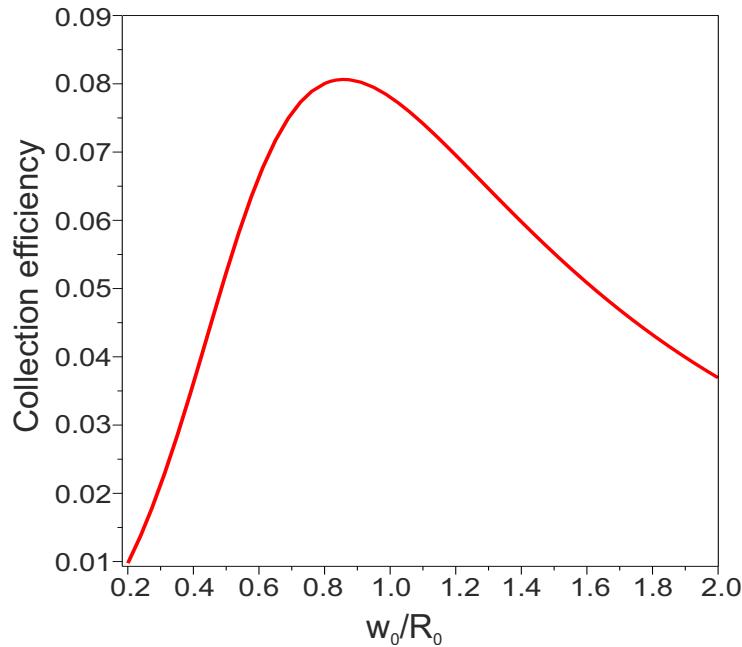
Figure 4.10.: Photon collection efficiency for the atomic dipole emitting H-polarized photons. The maximal collection efficiency is 8.07% with an optimal ratio of the waist w_0 of the collimator and the objective pupil radius R_0 of 85.44%.

The current state of the model is missing transverse and longitudinal displacement of the atom due to thermal effects. This needs to be considered in a future extension of the model and will reduce the achievable photon collection efficiency.

	Photon collection by the objective	Coupling efficiency into single mode fiber	Maximal photon collection efficiency
Point source approach	$4\pi \cdot 6.69\%$	80%	5.35%
Dipole emission characteristics	$4\pi \cdot 9.40\%$	86%	8.07%

Table 4.1.: Summarized results for the photon collection efficiency comparing the atomic emission pattern of a point source and dipole emission characteristics.

5. High NA microscope optical setup

The setup for the new microscope objective has to fulfill several functions. It must contain the necessary optics to overlap three wavelengths, from the ionization beam, dipole trap and fluorescence collection and the optical elements in order to perform the experiment under optimal conditions. The best performance is achieve for the case of maximal collection efficiency for the emitted photons by the trapped atom, strong focused dipole trap for trapping the atom and a fast and efficient ionization of the atom for the atomic state readout. The following chapter describes all the elements that are used in the setup and their characterized performance. Besides the quality of the optical elements that are used, it is crucial to match several alignment requirements in order to ensure diffraction limited operation of the new microscope objective. Several alignment techniques were elaborated for the setup and the methods will be explained in the following chapter. At the end of the chapter we will describe how we overlap the foci of the three wavelengths on the optical axis of the objective.

5.1. Optical setup

The microscope objective setup consists of three main components. The optical dipole trap laser for trapping the atom ($\lambda = 859$ nm), the fluorescence collection optics ($\lambda = 780$ nm) for collecting the emitted single photons of the ^{87}Rb atom during the entanglement generation process and the fluorescence light during the cooling procedure. Further the ionization laser ($\lambda = 473$ nm) is needed for the atomic state readout. All three wavelengths are focused by a confocal microscope objective to the center of the vacuum glass chamber. The optical dipole trap then determines the position of the atom. In order to have maximum collection of the scattered photons by the atom, it is crucial to overlap the focus of the fluorescence collection optics with the position of the atom and hence the dipole trap. In addition, the ionization laser needs to be focused on the same spot in order to have a maximal ionization rate, as it depends on the light intensity. The focusing is achieved by the new custom designed microscope objective[1] with an numerical aperture of 0.5 and a working distance of 14 mm. It is specified to be diffraction limited for all the three wavelengths and has a transmission of $> 90\%$. Further, it compensates for the 3.5 mm thick vacuum glass cell.

In order to test and characterize the setup in a separate lab, it was necessary to provide testing

---

[1]Photon Gear NIR Atom Imager
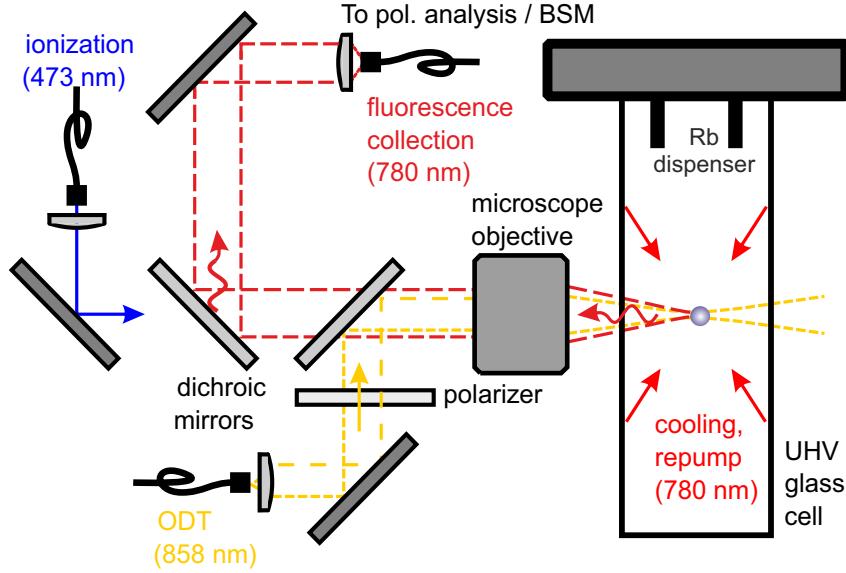
Figure 5.1.: Sketch of the optical setup for the new microscope objective which focusses the dipole trap and the ionization beam to the center of the vacuum glass cell. The fluorescence is collected by the same objective and coupled into a single-mode fiber. The dichroic mirrors separate the three different wavelenghts from the optical axis of the objective.

lasers, that correspond to the ones which are used in the main experiment (dipole trap and ionization). Therefore, we built up diode laser systems for each wavelength which are then connected to the respective fiber collimators of the new microscope objective setup. To simulate the fluorescence we use a laser which is counter-propagating to the actual fluorescence in the experiment. Hence we reverse the experimental scheme by focusing a 780 nm laser to the center of the vacuum glass cell. In this case, the focus size can be seen as a measure for the effective field of view of the fluorescence collection optics and thereby is a measure for the ability to collect the photons. Once the testing and alignment of the setup is completed, we will disconnect the fiber end which is connected to the lasers meanwhile keeping the end of the fiber in the collimators in order to preserve the alignment. Eventually, we will connect the fibers of the new objective setup with the fiber ends of the main experiment.

Another important component beside the microscope objective are the dichroic mirrors which superimpose the paths of all three wavelengths onto the optical axis of the microscope objective. The dichroic mirrors are coated in such a way that they either reflect or transmit the respective wavelength. In our setup we have two dichroic mirros. One of them is highly reflective for the dipole trap and highly transmissive for the ionization laser and the fluorescence collection. The other one is highly reflective for the fluorescence collection and highly transmissive for the ionization laser.

The entire structure for the new microscope objective is built on a separate breadboard. This design allows us to test, align and optimize the setup completely independent of the main exper-

iment, which is good for two reasons. First, the objective setup of the real experiment can still be used in the meantime in order to proceed with the experiment. Once the new setup is ready we will incorporate it in the real experiment by exchanging the two objective setups. Therefore, the height of the optical axis in the new setup is in agreement with the current setup. The other reason is that several tests and alignment procedures can't be executed in the environment of the real experiment, such as measuring and overlapping the foci of the three beams because the focal position is in the vacuum cell which makes it not possible to perform a knife-edge measurement. A schematic drawing of the microscope objective setup is shown in figure 5.1.

5.1.1. Laser optics

The following part describes each component of the setup, i.e. fluorescence collection, ionization laser and the optical dipole trap, and the corresponding optics in more detail. In particular, the key properties of each part that are crucial for the performance of the objective are elaborated.

5.1.1.1. Fluorescence collection - Spherical aberrations

Collimator - Monochromatic lens system   The beam size and the quality of it are essential parameters for our experiment, in particular for the fluorescence collection it determines how much of the NA of the microscope objective can be used and how much of the light that is collected by the objective can be coupled into the single mode fiber. For the fluorescence beam we considered two collimators. The first one is a monochromatic Schäfter-Kirchhoff collimator[2] with a focal length of 50 mm. The resulting beam size is 4.35 mm which corresponds to a Rayleigh length of $z_R = 76$ m. During the characterization of the beam quality, i.e. beam profiling with a CCD camera it was found, that this collimator induces severe spherical aberrations in the Gaussian beam profile. The shape of the distortion in the beam was dependent on the distance between the CCD camera and the collimator. Since these aberrations will have impact on the coupling efficiency for the light coming from the objective into the single-mode fiber after the collimator, it was necessary to asses the severity of the aberrations. For that we adapted an approach shown in [25] in order to quantify the aberrations, i.e. to find the parameters that describe the properties of the phase front of the electric field coming from the collimator.

A general description of the electric field of Laguerre-Gaussian modes when assuming a circular symmetric phase ($l = 0$) is given by:

$$E_{LG(p,l=0)} = E_0 \frac{w_0}{w(z)} exp\left(\frac{r^2}{w^2(z)}\right) L_P\left(\frac{2r^2}{w^2(z)}\right) exp\left(-ikz + ik\frac{r^2}{2R(z)} - i\xi(z)\right) \quad (5.1)$$

---

[2]60FC-L-4-M50L-02

where L_P denotes Laguerre gaussian mode, $R(z)$ the radius of the curvature of the beam's wavefront at position z and $\xi(z)$ the Guoy phase. The Guoy phase itself is given by:

$$\xi_p(z) = (2p - 1) \, arctan\left(\frac{z - z_0}{z_R}\right) \tag{5.2}$$

When we now assume the collimator to induce spherical aberrations due to lens imperfections, the electric field of the Gaussian beam after the collimator is given by:

$$E_{Coll.} = E_{LG(0,0)} \cdot exp\left(i\phi_{lens}\right) \cdot exp\left(i\phi_{abb.}\right) = \sum_{p=0}^{\infty} C_p E_{LG(p,l=0)} \tag{5.3}$$

with

$$\phi_{lens} = -\frac{kr^2}{2f}$$

being the phase shift induced on the Gaussian beam when propagating through a lens, and

$$\phi_{abb} = S\left(\frac{r^4}{w_0^4} - 2\frac{r^2}{w_0^2}\right)$$

describing the phase shift of the spherical aberrations with a parameter S, which denotes the strength of the aberrations. The spherical aberrations are caused by lens imperfection and as a result of the Gaussian beam transmitting through the lens, they are imprinted onto the phase of the electric field. Since the guoy phase is a function of the Gaussian mode, and the electric field itself is a function of the sum over all Gaussian modes, the difference in the Guoy phase of higher Gaussian modes $\Delta\xi$ induces the changes in the intensity profile in dependence of the propagation distance. Our experimental scheme in order to determine the S parameter consists of two steps. At first, we are measuring the intensity profiles of our Gaussian beam after the collimator at several distances where we see an evolution of the intensity distribution in the beam. Since the Rayleigh length of our collimated beam is 76 m which makes it complicated to track the intensity profile, we introduce a thin lens with a long focal length, assuming that the thin lens negligibly alters the spherical aberrations of the initial wavefront. By that it becomes more suitable to measure the intensity profile evolution of the beam at several positions around the focus. The second step is to simulate the evolution of the beam for several distances z and different strengths S by using diffraction integrals. By comparing the evolution of the intensity profile of the simulated- and experimental data, we can determine the corresponding parameter S, for which they have the best agreement (see figure 5.2). We found out, that for our collimator we get an estimate for the S parameter of 0.7. We want to stress here, that this approach only yielded an estimate for the parameter, since it can be seen that the agreement of data and simulation

is not perfect and it might need higher order terms of S to completely accurately describe the aberrations. However, the evolution of the shape distortion is alike from which we conclude that we give an estimate value for S.

With the determination of the severity of the spherical aberrations we are able to estimate the resulting overlap between the phase front created by the collimator and the Gaussian eigenmode of the fiber by calculating the overlap integral, as already discussed in Chapter 4. Since the Schäfter-Kirchhoff collimator, without considering the movement of the atom in the trap, only yields a coupling efficiency of 70%, we decided to use a different collimator.

Collimator - Spherical lens system The other fiber collimator[3] we characterized contains a four element, air-spaced spherical lens design with a focal length of 40mm. We characterized the beam again using again a lens with a long focal lens as described previously. However, we didn't see any distortion at any position around the focus. We concluded, that the spherical aberrations coming from the collimator are significantly smaller compared to the Schäfter-Kirchhoff aspheric lens collimator. This is why we eventually decided to use the beam with the better quality, however having a 0.7mm smaller waist. But as calculated in Chapter 4 this only costs us 5% of the coupling efficiency, which is why we rather use a collimator with a better beam quality. For future iterations of the objective setup, it is desirable to design a custom collimator with the optimal waist size according to our objective and without causing spherical aberration in order to maximize the coupling efficiency.

5.1.1.2. Optical dipole trap

The collimator[4] for the optical dipole trap contains a bi-aspheric lens and has a focal length of 18.4 mm. The waist that is created by this collimator has a size of $w_0 = 1.28$ mm before the objective. The beam parameters of the dipole trap before the objective and the define the trap geometry in the experiment, which in our case leads to a focal size of $2\,\mu$m corresponding to a Rayleigh length of $z_R = 13.6\,\mu$m at a wavelength of 859 nm. Unfortunately, also this collimator produces aberrations which lead to an asymmetric Gaussian profile before the objective. This can lead to deviations of the trap potential and the electric field distribution in the focus after the objective which will reduce the fidelity of the atomic state by disturbing the compensation mechanism of external magnetic fields [7]. In consequence drifts in the magnetic fields around the atom lead to energy shifts in the atomic state due to the Zeeman effect and thereby lead to a time evolution of the atomic state, which then reduces the fidelity. So far, we were not able to quantify the asymmetric Gaussian profile of the dipole trap beam before the objective. Furthermore, we couldn't see any significant asymmetry in the measurement of the dipole trap focus (see section 5.4). This could either be due to the fact that the aberration are not present in the focal area of

---

[3]Thorlabs C40FC-B
[4]Schäfter Kirchhoff 60-Fc-4-A18-02
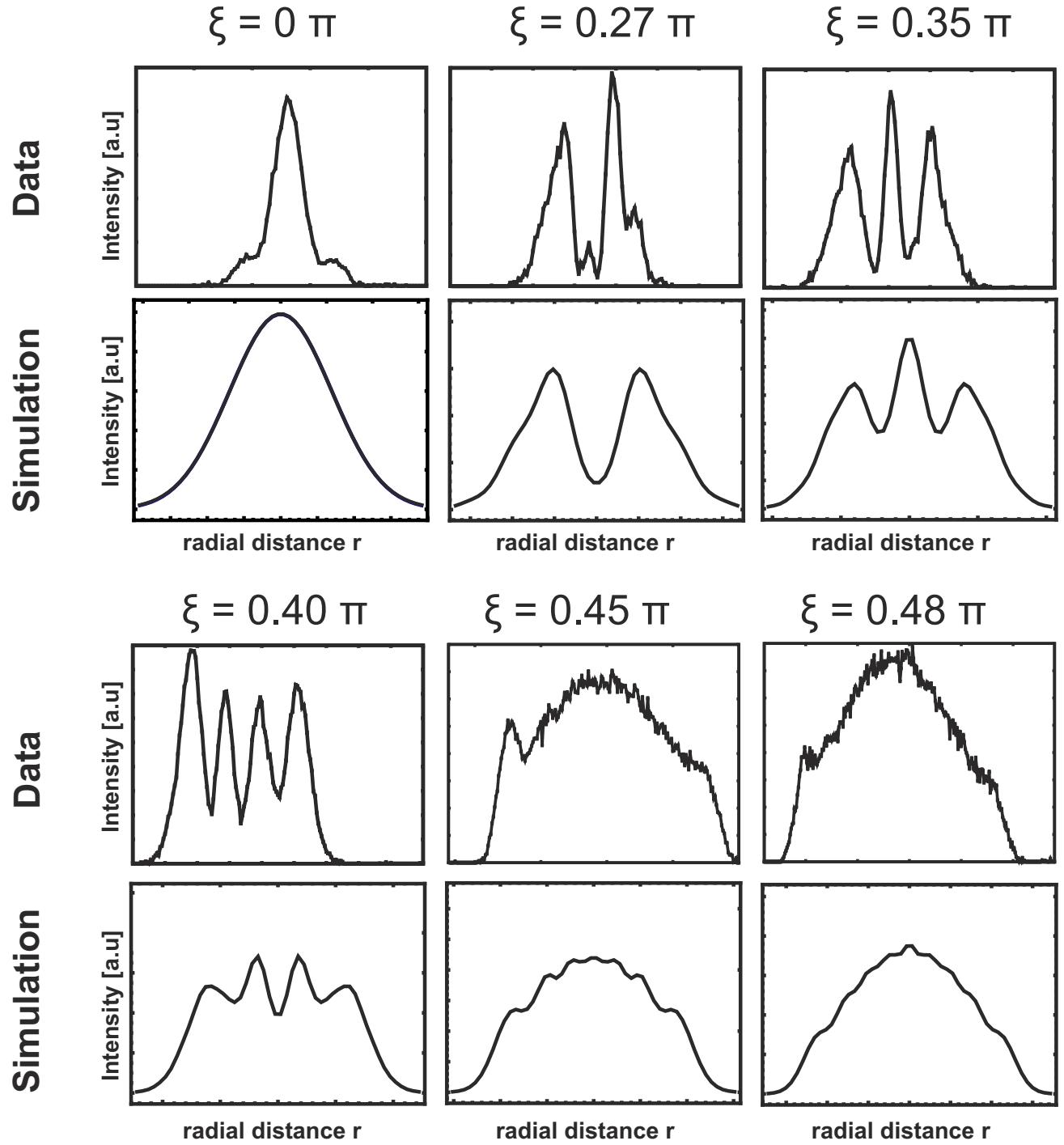
Figure 5.2.: Experimental and simulated intensity profiles for a gaussian beam with spherical aberrations at several positions as a function of the guoy phase. The plotted simulated data is for an S parameter of 0.7 which yielded the best agreement between measured- and simulated data.

the dipole trap. In that case the problem of the aberration are not crucial for us. Another reason for not seeing them in the focal area could be the way of our measurement. Since we use knife-edge method for measuring the focus, we effectively sum over the intensity distribution in every direction. This could misleadingly wash out the aberration effect in our focus measurement data while still being actually present. In any case it is recommended for future iterations to design the collimator custom and specifically adapting the needs of the experiments.

The choice of polarization for the dipole trap and its stability are crucial for the coherence time of the atomic state. As described in [7], it is thereby necessary to have a linear polarization of the dipole trap. This is provided by setting the polarization by a polarizer before the dichroic mirror which directs the dipole trap beam to the objective and after the broadband dielectric mirror[5] which is used to align the beam. The polarizer is chosen to only transmit H-polarized light with an extinction ratio of $\frac{1}{130000}$. It is also important to keep the intensity of the dipole trap as stable as possible. We do that, by using the small fraction of the light that gets transmitted through the otherwise high reflective dichroic mirror. Since the dichroic mirror has two layers, one being the anti-reflective coating and the other one being the dichroic filter, both layers produce transmission. The reflective coating transmits 0.69% and the dichroic filter 1.5% of the overall light intensity that is hitting the dichroic mirror. Since we have higher intensity in the dichroic filter transmission as in the reflective coating we use that light and focus it onto a fast photodiode which will in the main experiment be connected to a feedback loop to stabilize the laser power.

5.1.1.3. Ionization laser

The ionization laser has the weakest requirements in terms of beam quality, polarization preservation and transmission losses through the optical elements. It is operated at a wavelength of 473 nm. For collimation we also use a bi-aspheric lens system with a focal length of 18.4 mm. Again, we encounter spherical aberrations when using aspheric lenses. However, in the case of the ionization laser this doesn't have a large impact on the experiment. The only requirement we have is that there is enough power at the position of the atom in the trap in order to ionize the atom fast enough which will be the case if it is properly aligned. Thereby, we don't expect any major difficulties coming from the aberrations in the ionization beam if the alignment is good. However, the aberrations distort the beam profile in such a way, that it gets complicated to determine the center of the beam and thereby makes it hard to overlap it with other beams.

5.1.2. Dichroic mirrors

In order to superimpose the three laser beams onto the same optical path we use dichroic mirrors which are coated in such a way, that they either transmit or reflect the respective wavelength.

---

[5]Thorlabs BB1-E03

During transmission and reflection the dichroic mirrors have to fulfill two important requirements. First, the indistinguishability of the s- and p-polarized light, i.e. that the same fraction of both polarization is transmitted/reflected by the dichroic. This is specifically important for the fluorescence photons undergoing the BS-measurement, since we can only compensate for unitary transformations of the polarization without any losses. The information of the entangled atom-photon pair is stored in the polarization of the photon and the atomic state of the atom. Hence a non-unitary change of the polarization would alter the information and thereby reduce the fidelity of the atom-photon entanglement. Therefore, all dichroics are optimized for having identical s and p-polarization transmission and reflection for the respective wavelengths. As shown in figure 5.3, an equal transmission of s- and p-polarization is given with at least 99.9%.

The second important requirement is the absolute preservation of the polarization by the mirrors which is particularly important for the optical dipole trap. As discussed earlier, changes in the linear polarization of the dipole trap will reduce the coherence time of the atomic state. The preservation of the polarization of the dipole trap laser was measured in the following way (see figure 5.4). Directly after the fiber we maximize the fraction of H-polarization in the beam by using a $\lambda/2$-plate. The dichroic mirror was placed on a rotation stage in $45°$ to the incoming beam by aligning it to the row of hole of the breadboard. Right before the dichroic mirror we place a H-polarizer in order to fix the polarization to H and right after the dichroic mirror a V-polarizer to test the change of polarization by the dichroic mirror. Since in general polarizers not only absorb but also scatter the light of the polarization they filter out, it is important to measure the intensity not directly after the polarizer but at some distance. When now comparing the power before the dichroic mirror and after the V-polarizer we can calculate the extinction ratio, i.e. the ratio of light that doesn't change the polarization when being reflected by the dichroic mirror. Further we can calculate the angle by which the polarization is changed on the Bloch-sphere. As shown in figure 5.5, we repeat this for several angles of the dichroic mirror which is highly reflective for 850 nm. We find the optimal angle of incidence is at $45°$ with an extinction of 60000 and a maximal linear drift of the polarization of $0.26°$ on the Bloch sphere. These rates are sufficient for the stability of the dipole trap linear polarization. Further it shows, that our alignment precision for the angle of incidence on the dichroic mirror is not very critical.
The same measurement was repeated for the dichroic mirror using

5.2. Knife-edge method

The foci that we measure after the objective are in the order of 800 nm which makes it impossible to measure them with a CCD camera. Still, the measurement of the foci is mandatory for overlapping the three wavelengths on the same spot. Further, we will need it for the verification of our alignment method as discussed in section 5.3. Therefore we use a knife-edge method to determine the focal position and the focus size. The basic principle of a knife-edge method is that the total power in a beam is recorded while a sharp edge is translated through the beam (see figure 5.6). Our power recording device is a photodiode on which we place a gold structure
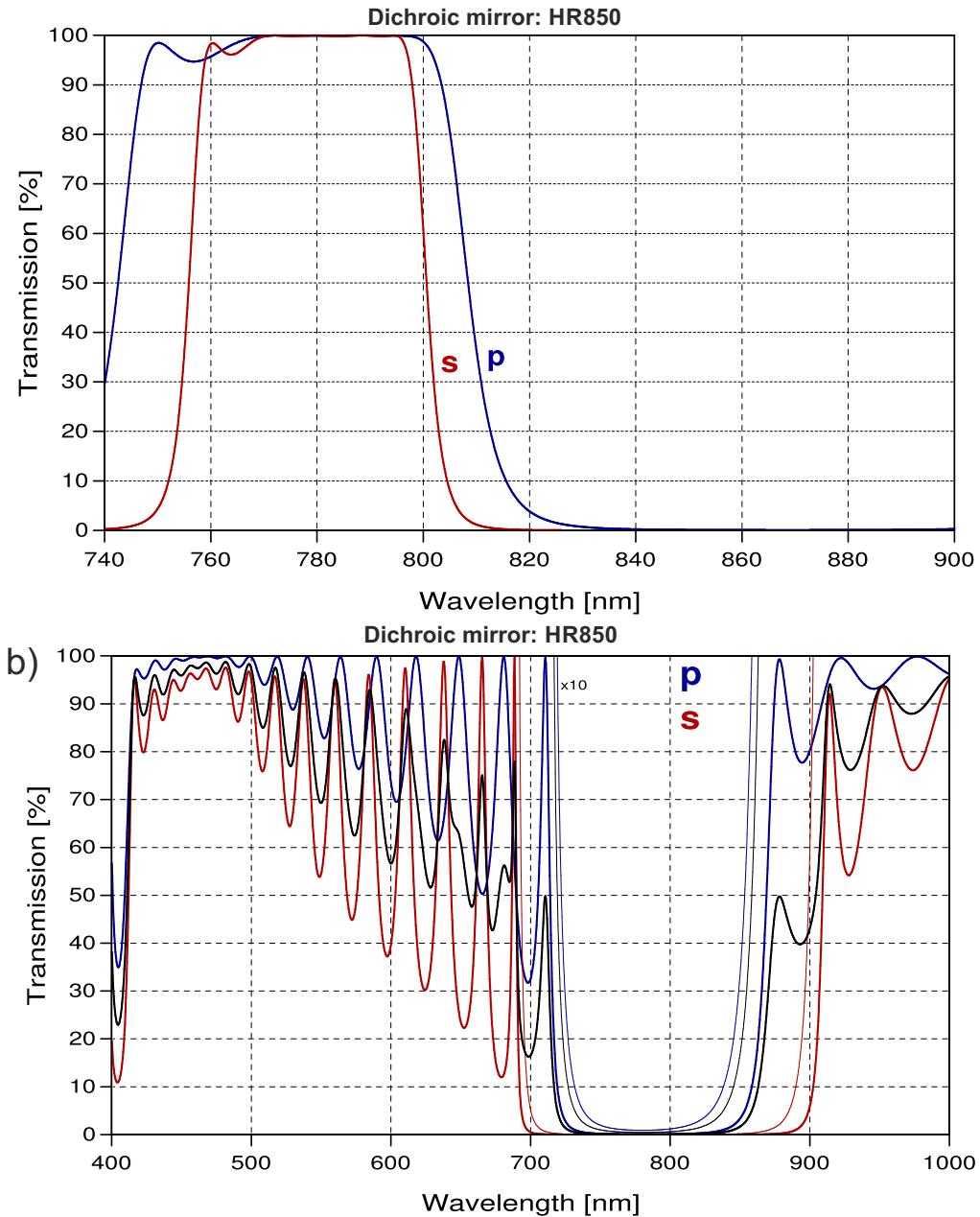
Figure 5.3.: a) Transmission of the s- and p-polarization on the dichroic that is high reflective for the dipole trap laser and high transmissive for the fluorescence collection. b) Transmission of the s- and p-polarization on the dichroic that is high reflective for the fluorescence collection and high transmissive for the ionization laser. In all cases, an equal transmission of s- and p-polarization is given with at least 99.9%.
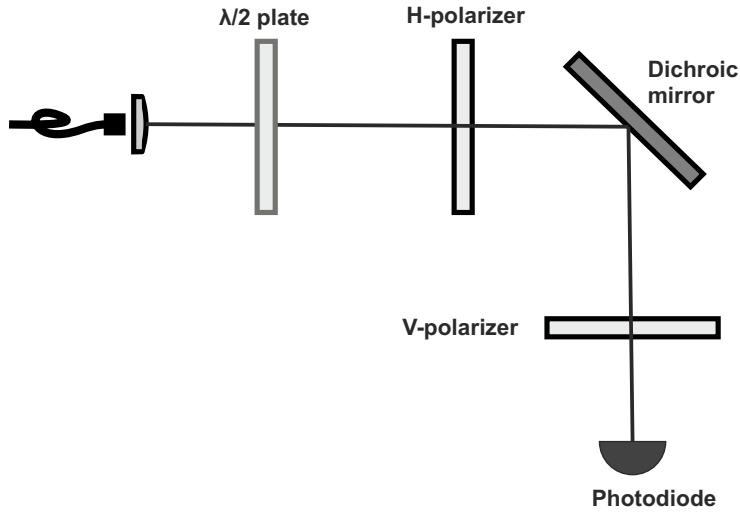
Figure 5.4.: The fraction of H-polarized light coming out of the fiber is maximized by a $\lambda/2$-plate. The first H-polarizer fixes the polarization and right after the dichroic mirror a V-polarizer to test the change of polarization by measuring the remaining intensity on a photodiode. The preservation was measured for several angles of the dichroic mirror.
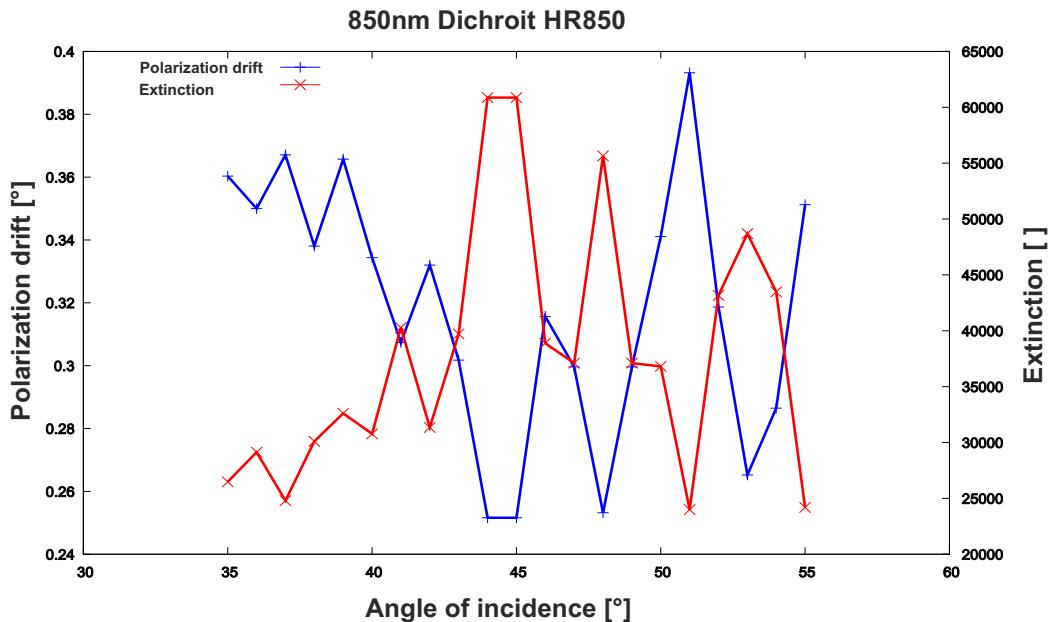
Figure 5.5.: Polarization preservation of the optical dipole trap beam after being reflected by the dichroic mirror for several angles of incidence. The graph shows extinction ratios and the corresponding change in polarization on the Bloch sphere. We get a minimum extinction ratio of $\frac{1}{25000}$ which is sufficient for the experiment.
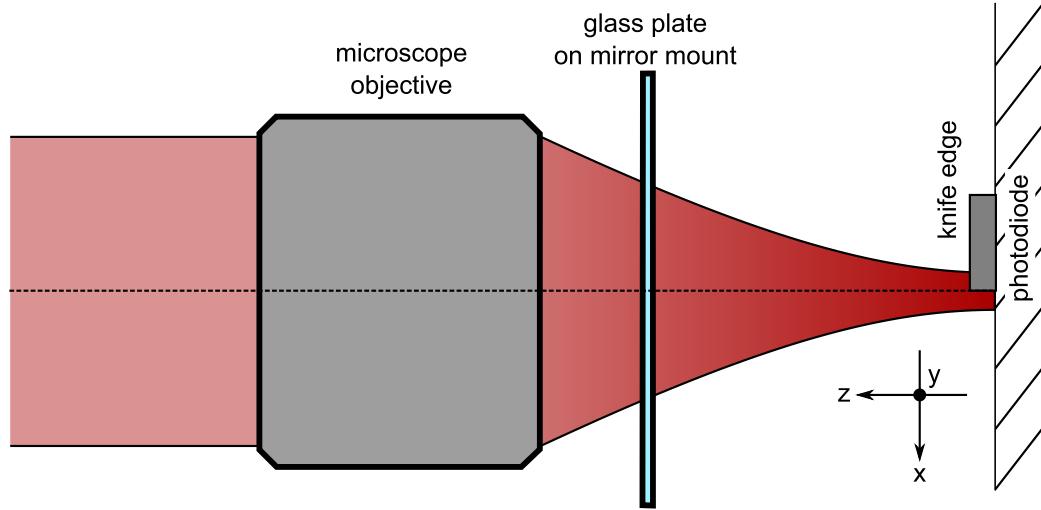
Figure 5.6.: Knife-edge method for measuring the foci after the objective. As a sharp edge we use a gold structure which is placed on a photodiode. The gold-structure is translated through the beam while the photodiode records the resulting intensity profile. From that we can reconstruct the Gaussian focus.

which defines the sharp edge. As a translation stage we use piezo motors in transverse direction and a step motor in longitudinal direction. Both have a possible step size of 20 nm. For a Gaussian beam, the integrated power as a function of the x position on the photodiode and a fixed y position is given by the following equation:

$$I(x) = y_0 + \frac{2P}{\pi w^2(z)} \int_{\infty}^{x} \int_{-\infty}^{\infty} e^{\frac{2(x^2 + y^2)}{w^2(z)}} = y_0 + y_1 erf(\frac{\sqrt{2}(x - x_0)}{w(z)} \qquad (5.4)$$

Where y_0 and y_1 are background light power and the power of the laser respectively. When now applying a least square fit with this function via the measured data, one obtains the Gaussian waist of the focus. By repeating this procedure at different longitudinal positions it is possible to determine the longitudinal focal position z_0 of the foci. This is done by fitting the function

$$w(z) = w_0 \sqrt{1 + \frac{M^4(z - z_0)^2}{z_R^2}} \qquad (5.5)$$

to the measured data for the waist $w(z)$ at different z-positions. The parameter M^2 describes how close a laser beam is to only contain single mode TEM_{00} parts, which in consequence is a measure for how small a beam can be focused [2].
An example for a scan in x-direction and a M^2 measurement is shown in figure 5.7.
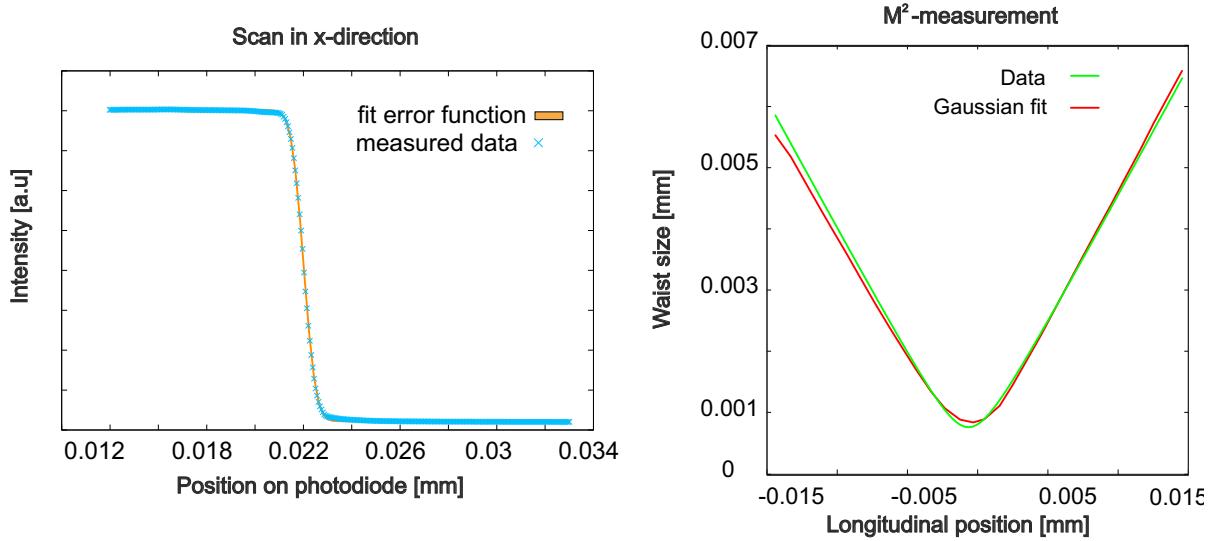
Figure 5.7.: Left) Knife-edge scan in x-direction. Right) M^2 measurement: repetition of a scan in x-direction for several focal position z.

This scheme for measuring the foci will be used throughout the remaining chapter at several parts.

5.3. Alignment requirements

For diffraction limited operation of the microscope objective we have to meet several alignment requirements. The following part describes the requirements and the method that we elaborated in order to achieve them.

5.3.1. Incoming beam

The first requirement concerns the angle between the incoming beam and the objective, which needs to be smaller than $1.37°$. This number derives from the specification of the objective by which it stills operates diffraction limited, for a displacement of the focus due to an angle in the incoming beam. Our approach in order to match this requirement is to overlap the incoming beam with its back reflection by introducing a mirror in front of the objective (see figure 5.8). This is done in the following way:

- The design of the objective is such that we can screw tube optics on the front side. By placing a mirror at the very end of the tube optics we ensure that the mirror is perpendicular
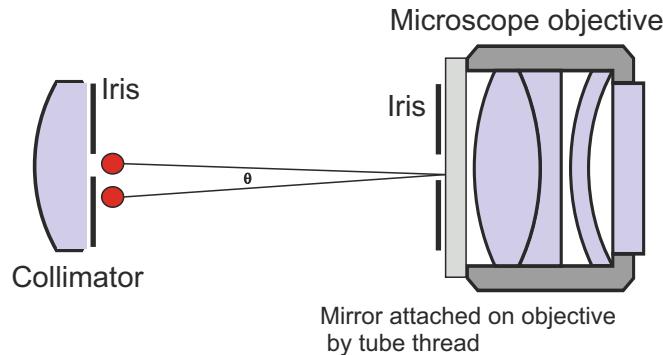
Figure 5.8.: Procedure for the alignment requirement of the incoming beam. Overlap the back reflection of the incoming beam by introducing a mirror in front of the objective.

to the optical axis. Further, we place an iris on the front side of the tube optics and another iris of the same size on top of our reference laser collimator, the fluorescence collection.

- In the next step we adjust the the height of the collimator and the objective to be in the same plane as the current microscope setup in the main experiment.

- The beam coming from the collimator needs to pass the center of the iris on the front side of the objective. The beam then gets reflected by the mirror back to the iris in front of the collimator. If the back reflected beam passes the center of the iris on the collimator, we achieve an estimated accuracy of $< 0.1°$ under the condition, that the mirror is perpendicular to the optical axis.

- The two remaining lasers are then overlapped with the reference laser by overlapping them on a CCD camera at 0.5m and 9m distance.

5.3.2. Glass cell

The second requirement concerns the alignment of the vacuum glass cell towards the objective which derives from the specification for the compensation of the glass thickness. The angle between the glass cell and the objective must be smaller than $\alpha < 0.1°$ (see figure 5.9). Our approach is to overlap the reflections coming from the objective and the glass cell and look at the resulting interference pattern. The detailed procedure is as follows:

- First we mount the glass plate on a translation stage right after the objective and fix it on a mirror mount. By that we are able to move the glass plate in longitudinal direction and we are able to introduce tilts in transversal direction.

- As a pre-alignment we move the glass as close to the objective, so that only a cleaning tissue with $50\mu m$ thickness fits between glass plate and objective. From that we move
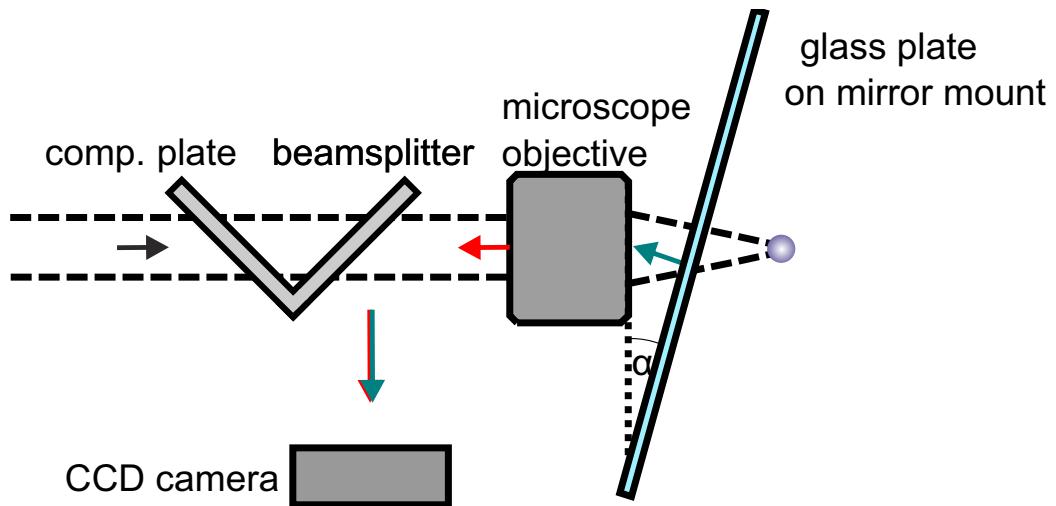
Figure 5.9.: Alignment scheme for the angle between the vacuum glass cell and the objective. By introducing a beamsplitter we overlap the reflections of the objective with the reflections coming from the vacuum glass plate on a CCD camera. The vacuum in the real experiment is mimicked for test purposes by an identical glass plate in terms of coating and thickness.

the glass plate 3 mm away from the objective which corresponds to the distance in the experiment.

- A beamsplitter and a compensation plate (to compensate for the path difference induced by the beamsplitter) are placed in front of the objective. An incoming beam produces back reflections from the objective and the glass plate which we overlap by means of the beamsplitter on a CCD camera (see figure 5.9).

- When now looking at the interference pattern in figure 5.10, we see two things. There are static concentric ring structures, i.e. they don't depend on the angle of the glass plate. They are interference fringes only coming from the lenses inside the objective. However, we see an additional interference pattern with less contrast, if there is an angle between glass plate and objective. Depending on the orientation of the angle, the interference fringes either go from top to bottom (horizontal tilt) or left to right (vertical tilt). A tilt of the glass plate in both directions result in diagonal interference fringes (as shown in the right picture in figure 5.10). The fringes become more visible when carefully pushing or pulling the breadboard which leads to a movement of the interference fringes.

- By the mirror mount we are able to adjust the glass plate in such a way, that we get rid of the additional interference pattern and hence also of the angle between glass plate and objective.

In the real experiment we won't have the possibility to easily tilt the vacuum glass chamber as we did in the test case, where the glass plate was placed on a mirror mount. Therefore, we
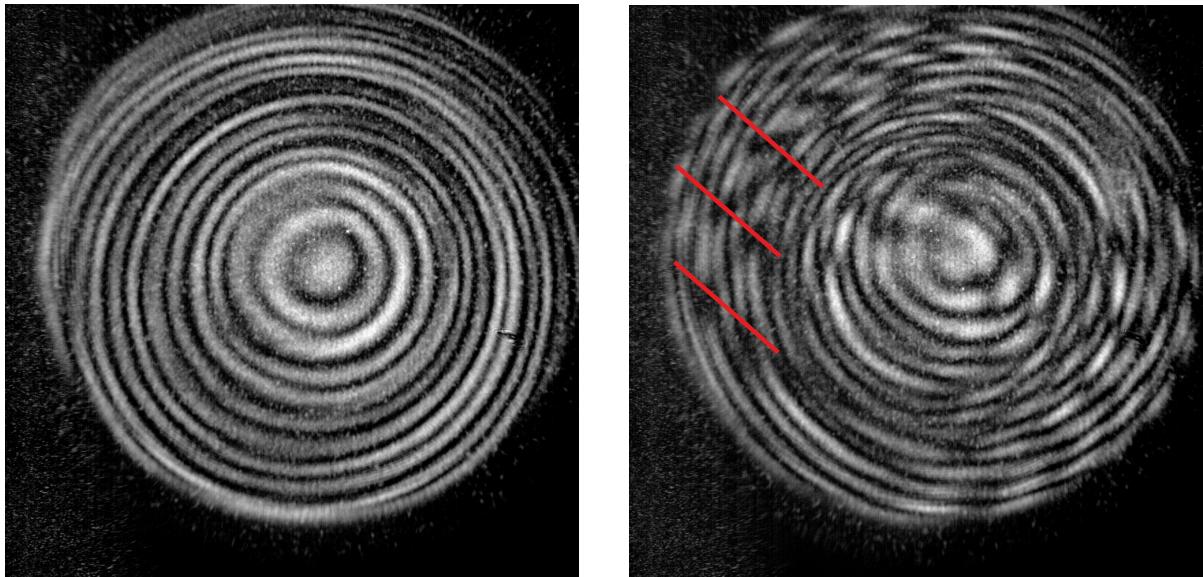
Figure 5.10.: Interference pattern for the overlapped back reflections coming from the objective and the glass plate. The left picture shows only the concentric ring structure which is independent of the orientation of the glass plate. The right side shows additional diagonal interference fringes coming from the interference of objective and glass plate back reflection.

designed two possible options for aligning the glass plate to the objective once inserted in the main experiment.

The first one is a wedge which we move below the breadboard in order to lift it up (see figure 5.11 (a)). The advantage is, that the stress induced on the breadboard is small which is good for the alignment preservation of the setup. The disadvantage is we can't place a wedge in front of the breadboard due to the geometry of the main experiment. This means, that depending on the angle direction we have to adjust, we may have to tilt the vacuum which is heavy and thereby unpractical.

The second approach is to use screws which are attached to the breadboard by a lever and pressed to the floor next to the breadboard (see figure 5.11 (b)) . When doing that at every side of the breadboard we are able to life it by adjusting the screws accordingly. The advantage of this method is the large degree of freedom we have for moving the breadboard. However, the stress on the breadboard due to the lever is large and might have impacts on the alignment which needs to be verified.

Verification of the alignment

So far we presented two alignment criteria for the incoming beam and the vacuum glass cell. However, we need verification, that we actually meet the alignment requirements for diffraction
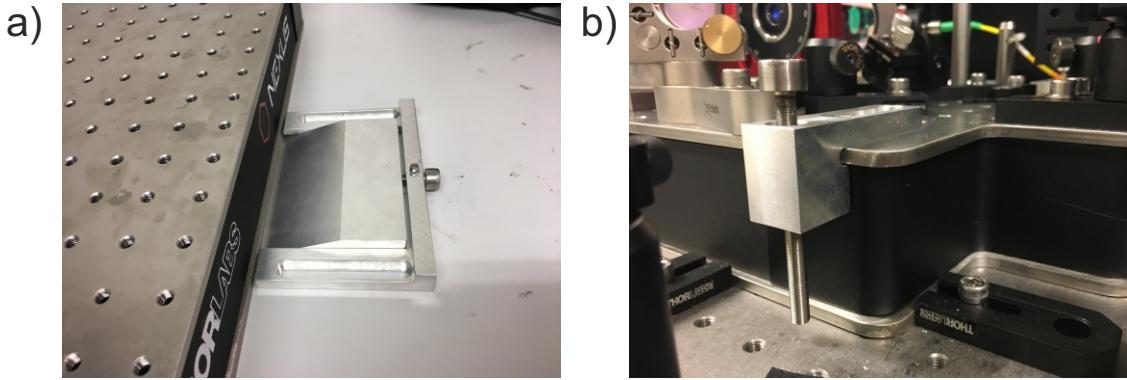
Figure 5.11.: Two options for lifting the breadboard in order to align the glass plate to the objective once the setup is inserted in the main experiment. (a) A wedge lifts the breadboard. (b) Screws on each side lift the breadboard.

limited operation of the objective. The condition for successful alignment is determined by the ability of the objective to focus the incoming beam into a high quality focus, i.e. minimized focal spot size and an almost Gaussian shaped focus. In order to verify our previous alignment approach we look at the focus after the objective. The focus is measured as described in section 5.2. Figure 5.12 shows a graph of such a measurement, where we record the total power in the beam after the objective as a sharp edge is translated through the beam using a piezo controlled translation stage. In our case the sharp edge is a gold structure which is placed on a photodiode. By that, we measure the intensity of the beam as a function of the position on the edge. Whenever the incoming beam is misaligned or the glass cell is tilted, the focus size will get larger and be smeared out at the edges as shown in figure 5.12. The smearing at the position of the focus depends on the corresponding tilt of the glass cell and the angle of the incoming beam respectively. This means we have a third condition for good alignment.

The procedure for verifying our alignment methods is as follows:

- Align the angle between glass plate and objective by looking at the focus after the objective. Adjust the glass plate until there is a minimal focus size and no smearing at the edges. The way to do that is to identify the threshold value in all directions, for which the induced tilt on the glass plate creates smearing of the focus and then adjust the glass plate exactly in the center of these limits. By the fine threaded screws at the mirror mount we are able to adjust the glass plate with a precision of $0.02°$.

- If the alignment method of looking at the interference pattern yields the same result, i.e. good alignment, the requirement on the alignment can be assumed to be matched. An example plot for a good focus measurement, after adjusting the glass plate is shown in figure 5.13.

Once the objective setup is incorporated in the main experiment we won't have the possibility to measure any foci inside the vacuum chamber. For that reason it is important to ensure, that with

a)

b)
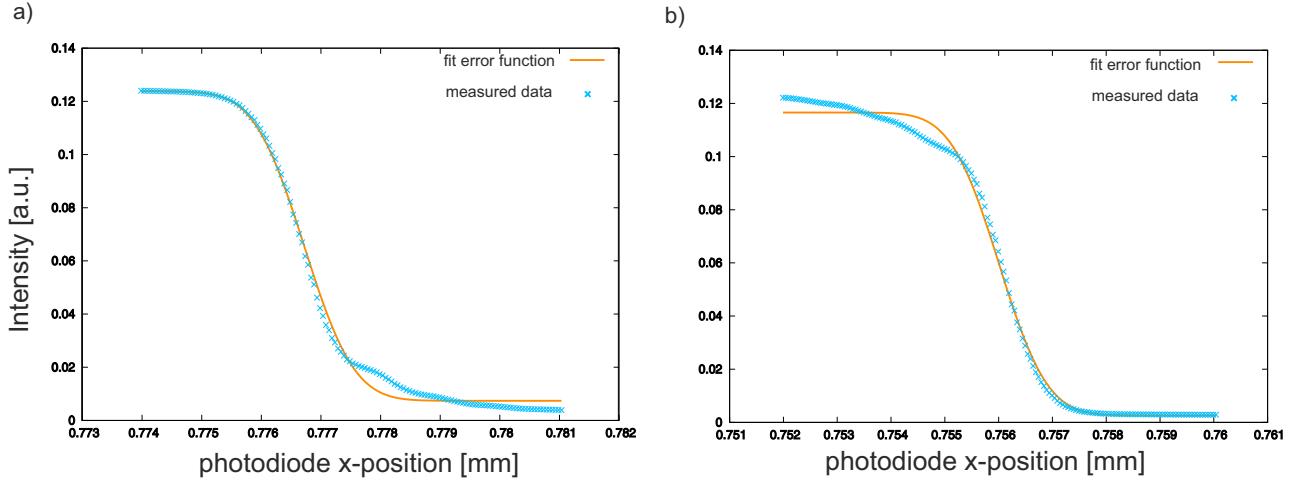
Figure 5.12.: Plots for the measured intensity as a function of the position on the photodiode in the focal plane. (a) The glass plate is tilted towards the objective which induces smearing at the edges of the focus (b) The glass plate is tilted in the opposite direction as in (a). The smearing happens then on the opposite side of the focus.

the alignment methods shown in part 5.3.1 and part 5.3.2 we are able to match the alignment requirements.

5.4. Overlapping the foci

The overlapping of the foci of the three wavelengths is essential for an optimal performance of the setup. As discussed in chapter 4, the photon collection efficiency is crucially reduced if the atom is displaced with respect to the optical axis. This is the case if the focus of the dipole trap which defines the position of the atom, is not overlapped with the photon collection optics. Additionally, the ionization beam needs to be overlapped with the dipole trap in order to provide fast and efficient ionization of the atom, which has an impact on the ionization time and thereby on the readout fidelity. Since the foci of the lasers are smaller than $1\mu m$, we use a knife-edge measurement as described in chapter 5.2.

In order to have a common focal point of the three wavelengths, the objective is designed in such a way, that the ionization beam needs to be divergent, the dipole trap convergent and the fluorescence collection collimated before the objective. We achieve that by using the the collection optics to be our collimated reference laser and adjust the collimation lenses of the other wavelengths accordingly. If the focus of one of the other lasers is closer to the objective, it is required to make the incoming beam more divergent and analogically, if the focus is after the reference focus, the incoming beam needs to be more convergent (see figure 5.14). Practically,
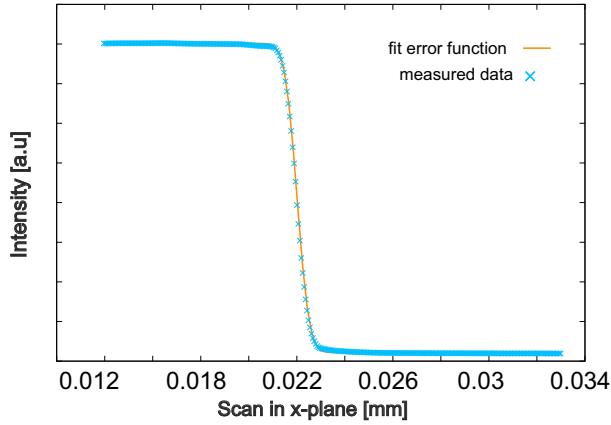
Figure 5.13.: Focus measurement after adjust the glass plate and the incoming beam. The focus has a Gaussian like shape and no smearing artifacts are visible. From that result we conclude that the alignment requirements are met.
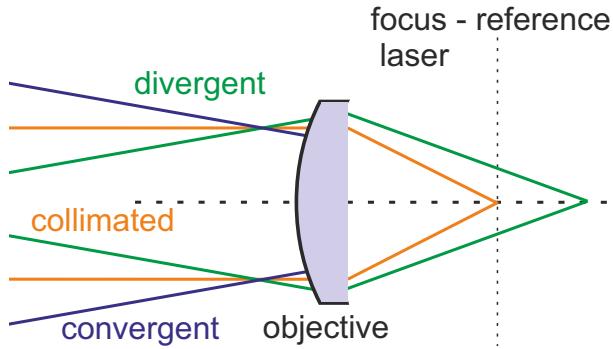
Figure 5.14.: The foci z-position of the three wavelengths may differ due to chromatic aberrations of the objective. This is resolved by adjusting the collimation lenses of the incoming beams depending on the foci displacement.

in order to move the focus closer to the objective it is necessary to expand the distance between the fiber end and the collimation lens. To move the focus further away of the objective, we need to shorten the distance between the fiber and the collimation lens.

Secondly, the foci may not be overlapped due to transverse displacement. This is caused by either an absolute offset or an angle between the incoming beams. In order to resolve this, we measure the foci at several z-positions and adjust the angle and offset of the incoming beam in such a way, that they overlap at all z-positions. Figure 5.15 and 5.16 show the final alignment with a M^2-measurement in horizontal and vertical direction. Plot a) shows the M^2 measurement and plot b) the vertical/horizontal position of the minimal Gaussian waist of the beam at each z-position. In z-direction, the foci overlap up to a precision of 300 nm. The difference in the absolute z-position value differs for a vertical and horizontal scan direction. The reason for

that isn't yet completely understood. Either, the focus of all wavelengths has an astigmatism or there is a problem with the definition of the absolute position in the measurement apparatus. However, the foci are overlapped in z-direction for both measurement directions, which is the crucial criterion for the performance of the setup. Further, the foci are overlapped in transverse direction with a precision of 50 nm in x- and y-direction. The transverse overlap of the beams remains basically the same for different z-positions, which indicates that they are parallel to each other. The drift of the vertical position may be due to a tilt in the mounting of the photodiode. The sudden drift of the horizontal position after the focus can't be explained yet. The results of the measurements are given in table 5.1.

Wavelength	$z_{0,x}(nm)$	$z_{0,y}(nm)$	$x_0(nm)$	$y_0(nm)$	$\bar{w}_0(nm)$	M^2
780 nm	0	0	0	0	774	1.2
859 nm	200 ± 100	200 ± 100	50 ± 30	50 ± 30	2058	1.1
473 nm	300 ± 100	200 ± 100	25 ± 30	30 ± 30	664	1.1

Table 5.1.: Precision of the final alignment result for the fluorescence optics, dipole trap and ionization beam. The fluorescence optics is defined as the reference beam and hence defined as the zero point.

Conclusion

The overlapping of the foci is an important measure for the expected performance of the new microscope objective. In particular the size of focus of the fluorescence collection gives an indication on the amount of photons that can be collected by the objective. The measured focus of 774 nm is the smallest focus that was so far measured for the experiment (compare [19]) and among other reasons gives hope for a significant improvement on the collection efficiency. Further, we don't expect to have significant losses for the coupling efficiency due to our alignment precision. As calculated in 4, we expect to loose 5% by a displacement of 50 nm in transverse direction and 2% in by a displacement of 300 nm, which is the limit of our experimental ability to overlap the beams.

5.4.1. Future verification of the alignment

After successful alignment of the microscope objective setup, we need to incorporate it in the main experiment. During the transportation process and commissioning of the setup, it may happen that in particular the transverse alignment drifts from the previously overlapped configuration which was achieved during the knife-edge alignment process. Therefore, while still being optimal aligned, we measure the beam profile of the three wavelengths before the objective by introducing a mirror in front of the objective. This is done exemplary shown here for the near field at a distance of 0.5 m and for the far field at 3m distance. For the fluorescence collection we determine the center of mass of the intensity distribution and keep the it as a reference position
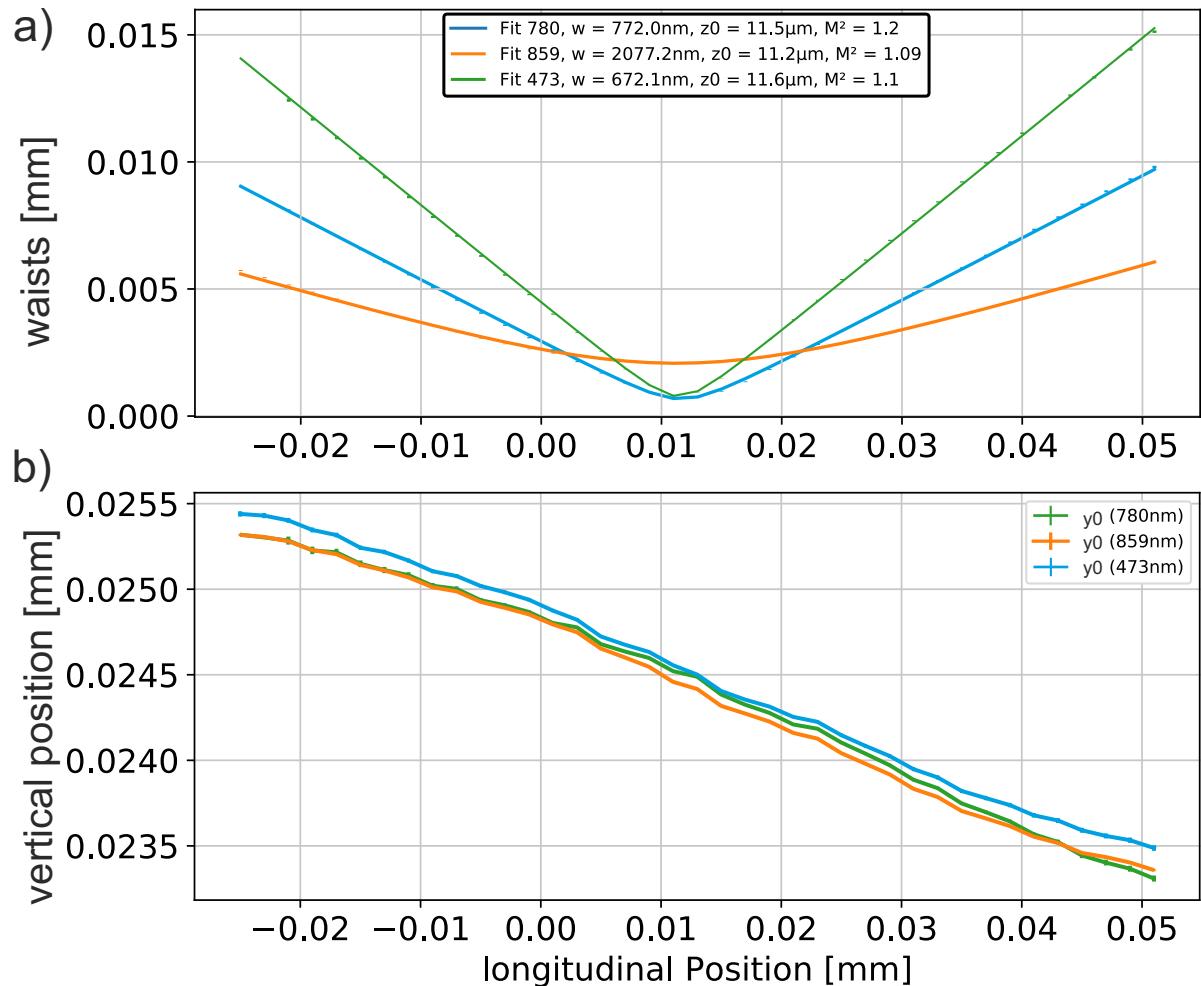
Figure 5.15.: Final focus scan in vertical direction. Plot a)M^2 measurement - Beam radius w(z) measured for several longitudinal positions for fluorescence collection (blue) dipole trap (orange) and ionization beam (green) with a least square fit to the measured data. The foci are overlapped in z-direction with an accuracy of 300 nm Plot b) shows the corresponding vertical positions for the respective w(z). The three beams are overlapped with an accuracy of 50 nm.
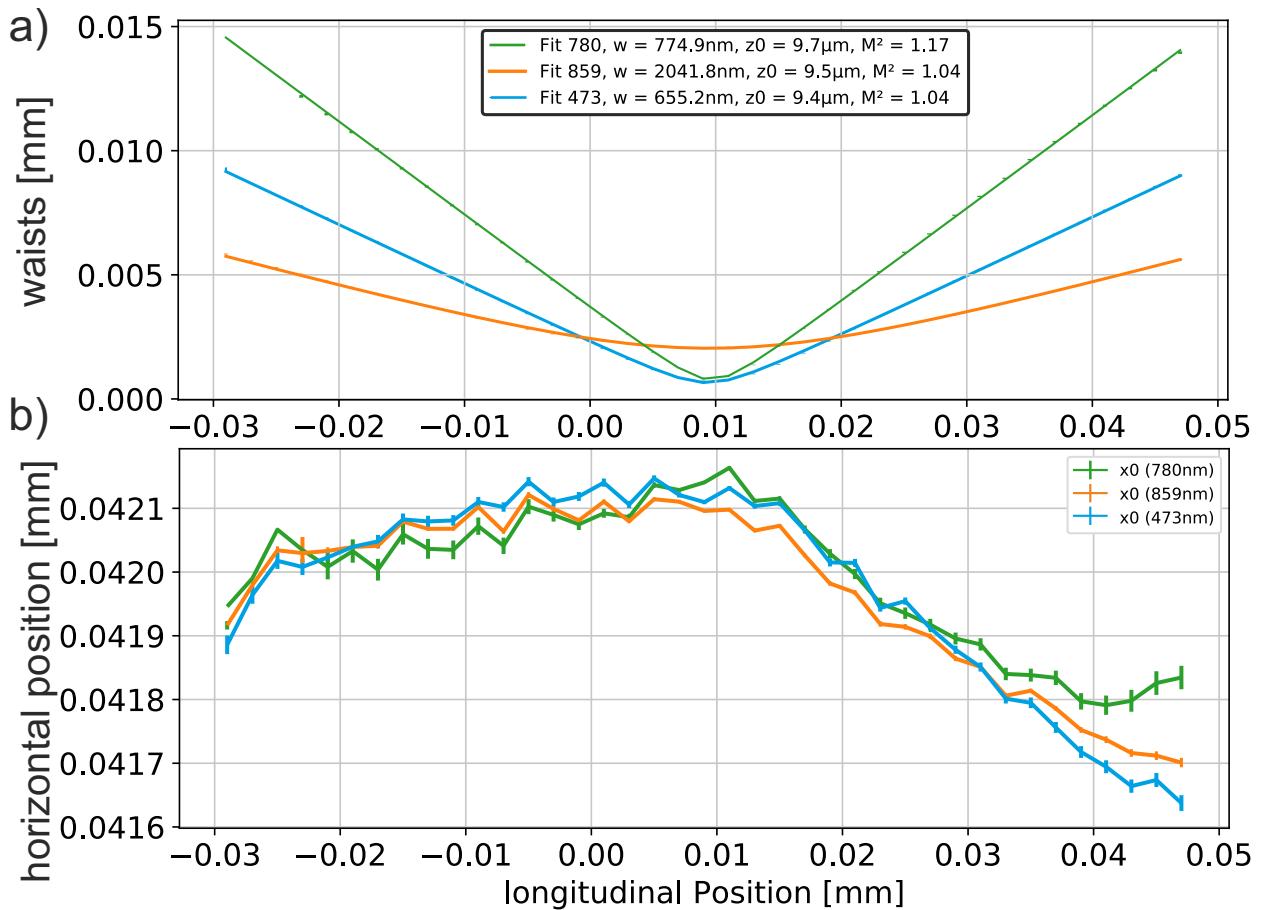
Figure 5.16.: Final focus scan in horizontal direction. Plot a)M^2 measurement - Beam radius w(z) measured for several longitudinal positions for fluorescence collection (blue) dipole trap (orange) and ionization beam (green) with a least square fit to the measured data. The foci are overlapped in z-direction with an accuracy of 300 nm Plot b) shows the corresponding horizontal positions for the respective w(z). The three beams are overlapped with an accuracy of 50 nm.

on the camera. From figure 5.17 it can be seen, that the center of mass of the other beams is at first sight not the same as for the reference laser, even though well aligned when performing a knife-edge measurement. However, it is not trivial to overlap the beams by only using the beam profiling since beams are aberrated and not collimated. Hence, figure 5.17 gives a useful reference for future verification of the transverse alignment by overlapping the beams on a CCD camera, once the setup is incorporated in the main experiment.
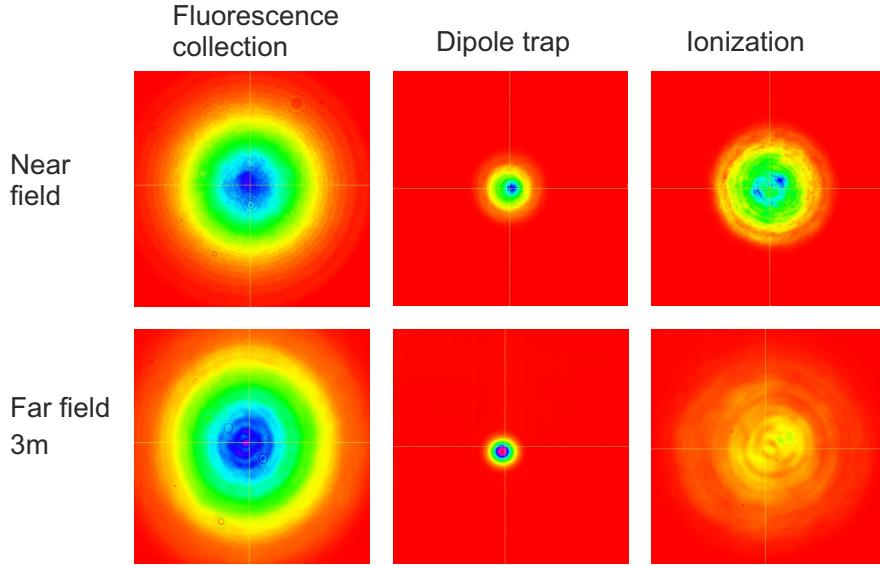
Figure 5.17.: Beam profile of the three beams before the objective in the near (0.5m) and far field (3m). The cross determines the center of mass of the intensity distribution of the fluorescence collection. It can be seen, that for the overlapped case, the relative position of the two remaining beams is slightly displaced. This gives an indication for future alignment verification.

5.4.2. Strongly focused beams

The waist sizes of the foci measured in section 5.4 are not in agreement with the theoretical waist size for Gaussian optics after a focusing lens. The following section discusses two issues which can lead to a deviation from the paraxial expectation for the waist size in the focus. In Gaussian optics, the minimal waist size for a Gaussian beam after a focusing lens is given by:

$$w_0 = \frac{\lambda \cdot f}{\pi \cdot w} \tag{5.6}$$

where λ is the wavelength, f the focal length and w the waist of the beam before the lens. The theoretical waist for the fluorescence collection laser is 689 nm which clearly differs from the

measured value of 774 nm. There are several reasons for not measuring the expected waist size for Gaussian optics:

- The formulation of Gaussian optics in the paraxial approximation isn't valid for a Gaussian beam which is focused to very small spot sizes in the order of the wavelength. However, the foci of the beams in our experiment are in the order of $600 - 800$ nm. Hence, the paraxial approximation is not valid for the large divergence angles. A more accurate description of strong focused laser beams can be found in [6, 21] and in particular for Gaussian beams in [22].

- The interaction of highly focused linearly polarized optical beams with a knife-edge induces material dependent spatial shifts of the reconstructed intensity distribution due to plasmonic effects. As described in [20] this is caused by interaction of the highly focused beam with the eigenmodes of the metal-insulator-metal-structure of the knife-edge material.

Ultimately, it is difficult to combine all of the effects to an expected value for the waists sizes. However, we expect that the discrepancy in the waist size doesn't impact the quality of the overlapping result and hence will induce no reduction of the setup performance.

6. Summary and Outlook

This thesis describes the characterization and experimental steps for the implementation of a new high NA microscope objective for increasing the photon collection efficiency of the current experiment. This is an essential ingredient for increasing the atom-atom entanglement event rate which is necessary for generating entanglement over longer-distances.

The first part of the thesis discusses aspects on the general photon collection rate of the objective and the subsequent coupling into a single mode fiber with a Gaussian eigenmode. Assuming polarized photons, it was found that maximally 8.07% of all photons emitted by the atom can be coupled into the single mode fiber with an optimal waist to objective pupil ratio of 85.44%. This would yield an enhancement of the photon collection efficiency by a factor of 8.7 compared to the current rate. Limiting factors for the photon collection efficiency are the quality of the optics, as for example the fiber collimator and thermal movement of the atom in the trap.

The second part describes experimental details of the new microscope objective setup which contains the optical dipole trap, the ionization beam and the optics for the fluorescence collection. All the used elements in the setup are described and the performance is characterized. By means of a knife-edge method we are able to measure the foci after the objective, which are in the order of 800 nm. Thereby, we are able to overlap the three wavelengths with a precision of 300 nm in longitudinal direction and 50 nm in transverse direction. The overlap precision and the size of the foci are a promising hint on a significant enhancement of the photon collection efficiency.

Outlook

The characterization of the new microscope objective setup and the calculations on the possible photon collection efficiency improvements have to be verified in the actual experiment. Therefore, it is necessary to incorporate the setup into the main experiment. After that, the experimental scheme for atom-atom entanglement has to be performed with the new objective, which includes trapping single atoms and detecting single photons coming from the spontaneous emission process of the atom. After upgrading both labs with a new microscope objective, it becomes possible to measure the actual enhancement factor on the atom-atom entanglement event distribution. That measurement will finally validate our effort to optimize the performance of the microscope objective setup and is the experimental prove for our alignment techniques and the characterization of the optics.

The other important step on our route for long-distance entanglement of atoms is to frequency

convert the photons to the telecom waveband. After a successful and efficient conversion, including the preservation of important single photons properties such as the coherence times, it will be possible to transmit photons through an optical fiber with low attenuation of the signal. The upgrade to a high NA custom designed microscope objective and the optimization of the objective setup combined with a frequency conversion of the photons is an important step towards longer distances of atom-atom entanglement rate. Including the proposed and realized improvements it will be possible to create atom-atom entanglement over distances on the order of 20 km at a reasonable event rate.

A. Dipole emission characteristics - Calculations

Calculations for the derivation of the normalized electric field components of the atomic dipole emission characteristics:

$$E_H(x, y, z) = \frac{e^{ikr}}{r} \frac{1}{\sqrt{1 - sin^2\theta \cdot cos^2\varphi}} \cdot \sqrt{cos(\theta)} \cdot \begin{pmatrix} \sqrt{\frac{3}{4\pi}} \cdot (cos^2\theta + sin^2\theta \cdot sin^2\varphi) \\ -\sqrt{\frac{3}{\pi}} \cdot sin^2\theta \cdot sin\varphi \cdot cos\varphi \\ -\sqrt{\frac{3}{\pi}} \cdot sin\theta \cdot cos\theta \cdot cos\varphi \end{pmatrix} \quad \text{(A.1)}$$

$$= \frac{e^{ik\sqrt{x^2+y^2+z^2}}}{(x^2+y^2+z^2)^{\frac{3}{2}}} \cdot \frac{1}{\sqrt{1 - \frac{x^2}{(x^2+y^2+z^2)}}} \cdot \frac{\sqrt{z}}{(x^2+y^2+z^2)^{\frac{1}{4}}} \begin{pmatrix} \sqrt{\frac{3}{4\pi}} \cdot (y^2 + z^2) \\ -\sqrt{\frac{3}{\pi}} \cdot y \cdot x \\ -\sqrt{\frac{3}{\pi}} \cdot z \cdot x \end{pmatrix}$$

$$\frac{e^{ik\sqrt{x^2+y^2+z^2}}}{(x^2+y^2+z^2)^{\frac{3}{2}}} \cdot \sqrt{\frac{x^2+y^2+z^2}{y^2+z^2}} \cdot \frac{\sqrt{z}}{(x^2+y^2+z^2)^{\frac{1}{4}}} \begin{pmatrix} \sqrt{\frac{3}{4\pi}} \cdot (y^2 + z^2) \\ -\sqrt{\frac{3}{\pi}} \cdot y \cdot x \\ -\sqrt{\frac{3}{\pi}} \cdot z \cdot x \end{pmatrix}$$

$$\frac{e^{ik\sqrt{x^2+y^2+z^2}} \sqrt{z}}{(x^2+y^2+z^2)^{\frac{5}{4}} \sqrt{y^2+z^2}} \cdot \begin{pmatrix} \sqrt{\frac{3}{4\pi}} \cdot (y^2 + z^2) \\ -\sqrt{\frac{3}{\pi}} \cdot y \cdot x \\ -\sqrt{\frac{3}{\pi}} \cdot z \cdot x \end{pmatrix}$$

$$E_V(x, y, z) = \frac{e^{ikr}}{r} \cdot \frac{1}{\sqrt{cos^2\theta + sin^2\theta \cdot cos^2\varphi}} \cdot \sqrt{cos(\theta)} \cdot \begin{pmatrix} -\sqrt{\frac{3}{\pi}} \cdot sin^2\theta \cdot sin\varphi \cdot cos\theta \\ \sqrt{\frac{3}{4\pi}} \cdot (sin^2\theta \cdot cos^2\varphi + cos^2\theta) \\ -\sqrt{\frac{3}{\pi}} \cdot cos\theta \cdot sin\theta \cdot sin\varphi \end{pmatrix}$$

$$\text{(A.2)}$$

$$= \frac{e^{ik\sqrt{x^2+y^2+z^2}}}{(x^2+y^2+z^2)^{\frac{3}{2}}} \cdot \frac{(x^2+y^2+z^2)^{\frac{3}{2}}}{\sqrt{\frac{z^2}{x^2+y^2+z^2} + \frac{x^2}{x^2+y^2} \cdot \frac{x^2+y^2}{x^2+y^2+z^2}}} \cdot \frac{\sqrt{z}}{(x^2+y^2+z^2)^{\frac{1}{4}}} \cdot \begin{pmatrix} -\sqrt{\frac{3}{\pi}} \cdot y \cdot x \\ \sqrt{\frac{3}{4\pi}} \cdot (x^2+z^2) \\ -\sqrt{\frac{3}{\pi}} \cdot z \cdot y \end{pmatrix}$$

$$\frac{e^{ik\sqrt{x^2+y^2+z^2}}}{(x^2+y^2+z^2)^{\frac{3}{2}}} \cdot \frac{\sqrt{x^2+y^2+z^2}}{\sqrt{z^2+x^2}} \cdot \frac{\sqrt{z}}{(x^2+y^2+z^2)^{\frac{1}{4}}} \cdot \begin{pmatrix} -\sqrt{\frac{3}{\pi}} \cdot y \cdot x \\ \sqrt{\frac{3}{4\pi}} \cdot (x^2+z^2) \\ -\sqrt{\frac{3}{\pi}} \cdot z \cdot y \end{pmatrix}$$

$$\frac{e^{ik\sqrt{x^2+y^2+z^2}}\sqrt{z}}{(x^2+y^2+z^2)^{\frac{5}{4}}\sqrt{x^2+z^2}} \cdot \begin{pmatrix} -\sqrt{\frac{3}{\pi}} \cdot y \cdot x \\ \sqrt{\frac{3}{4\pi}} \cdot (x^2+z^2) \\ -\sqrt{\frac{3}{\pi}} \cdot z \cdot y \end{pmatrix}$$

$$E_\pi(x,y,z) = \frac{e^{ikr}}{r} \cdot \frac{1}{sin^2\theta} \cdot \sqrt{cos(\theta)} \cdot \begin{pmatrix} -\sqrt{\frac{3}{\pi}} \cdot sin\theta \cdot cos\theta \cdot cos\varphi \\ -\sqrt{\frac{3}{\pi}} \cdot sin\theta \cdot cos\varphi \cdot sin\varphi \\ \sqrt{\frac{3}{4\pi}} \cdot sin^2\theta \end{pmatrix} \quad (A.3)$$

$$\frac{e^{ik\sqrt{x^2+y^2+z^2}} \cdot \sqrt{z}}{(x^2+y^2+z^2)^{\frac{5}{4}} \cdot \sqrt{x^2+y^2}} \cdot \begin{pmatrix} -\sqrt{\frac{3}{\pi}} \cdot z \cdot y \\ -\sqrt{\frac{3}{\pi}} \cdot z \cdot x \\ \sqrt{\frac{3}{4\pi}} \cdot (x^2+y^2) \end{pmatrix}$$

Bibliography

[1] A.K.Ekert. Quantum cryptography based on bell's theorem. *Phys. Rev. Lett*, 1991.

[2] B.E.A.Saleh and M.C.Teich. *Fundamentals of photonics*. 2007.

[3] J. Bell. On the einstein-podolsky-rosen paradox. *Physics*, 1964.

[4] C. H. Bennett, G. Brassard, C. Crepeau, R. Jozsa, A. Peres, and W. K. Wootters. Teleporting an unknown quantum state via dual classical and einstein-podolsky-rosen channels. *Phys. Rev. Lett*, 1993.

[5] M. Bock, P. Eich, S. Kucera, M. Kreis, A. Lenhard, C. Becher, and J. Eschner. High-fidelity entanglement between a trapped ion and a telecom photon via quantum frequency conversion. *NATURE COMMUNICATIONS*, 2018.

[6] A. Bovin and E. Wolf. Electromagnetic field in the neighborhood of the focus of a coherent beam. *Phys. Rev. Lett 138*, 1965.

[7] D. Burchard. *A Rigorous Test of Bells Inequality and Quantum Teleportation Employing Single Atoms*. PhD thesis, 2018.

[8] B. G. Christensen, K. T. McCusker, J. B. Altepeter, B. Calkins, T. Gerrits, A. E. Lita, A. Miller, L. K. Shalm, Y. Zhang, S. W. Nam, N. Brunner, C. C. W. Lim, N. Gisin, and P. G. Kwiat. Detection-loophole-free test of quantum nonlocality, and applications. *Phys. Rev. Lett.*, 111:130406, Sep 2013.

[9] S. Chu, L. Hollberg, J. E. Bjorkholm, A. Cable, and A. Ashkin. Three-dimensional viscous confinement and cooling of atoms by resonance radiation pressure. *Phys. Rev. Lett*, 1985.

[10] J. F. Clauser, M. A. Horne, A. Shimony, and R. A. Holt. Proposed experiment to test local hidden-variable theories. *Phys. Rev. Lett 23*, 1969.

[11] A. Einstein and M. Born. *Briefwechsel*. 1915.

[12] A. Einstein, B. Podolsky, and N. Rosen. Can quantum-mechanical description of physical reality be considered complete? *Phys. Rev., 47:777-780*, 1935.

[13] Marissa Giustina, Marijn A. M. Versteegh, Sören Wengerowsky, Johannes Handsteiner, Armin Hochrainer, Kevin Phelan, Fabian Steinlechner, Johannes Kofler, Jan-Åke Larsson, Carlos Abellán, Waldimar Amaya, Valerio Pruneri, Morgan W. Mitchell, Jörn Beyer, Thomas Gerrits, Adriana E. Lita, Lynden K. Shalm, Sae Woo Nam, Thomas Scheidl, Rupert Ursin, Bernhard Wittmann, and Anton Zeilinger. Significant-loophole-free test of bell's theorem with entangled photons. *Phys. Rev. Lett.*, 115:250401, Dec 2015.

[14] R. Grimm, M. Weidemuller, and Y. B. Ovchinnikov. Optical dipole traps for neutral atoms. *Advances in Atomic Molecular and Optical Physics*, 2000.

[15] T. W. Haensch and A. L. Schawlow. Cooling of gases by laser radiation. *Optics Communication*, 1975.

[16] B. Hensen, H. Bernien, A. E. Dreau, A. Reiserer, N. Kalb, M. S. Blok, J. Ruitenberg, R. F. L. Vermeulen, R. N. Schouten, C. Abellan, W. Amaya, V. Pruneri, M. W. Mitchell, M. Markham, D. J. Twitchen, D. Elkouss, S. Wehner, T. H. Taminiau, and R. Hanson. Loophole-free bell inequality violation using electron spins separated by 1.3 kilometres. *Nature, 526*, 2015.

[17] J. D. Jackson. *Classical electrodynamics*. 1962.

[18] K.Mattle, H.Weinfurter, P.G.Kwiat, and A.Zeilinger. Dense coding in experimental quantum communication. *Phys. Rev. Lett*, 1996.

[19] N. Ortegel. *State readout of single Rubidium-87 atoms for a loophole-free test of Bell's inequalities*. PhD thesis, 2016.

[20] P.Marchenko, S.Orlov, C.Huber, P.Banzer, S.Quabis, U.Peschel, and G.Leuchs. Interaction of highly focused vector beams with a metal knife-edge. *arXiv:1102.2140v3*, (2011).

[21] R. Richards and E. Wolf. Proc. roy. soc. *Proc. Roy. Soc. A 253*, 1959.

[22] W. Rosenfeld. *Experiments with an Entangled System of a Single Atom and a Single Photon*. PhD thesis, 2008.

[23] Wenjamin Rosenfeld, Daniel Burchardt, Robert Garthoff, Kai Redeker, Norbert Ortegel, Markus Rau, and Harald Weinfurter. Event-ready bell test using entangled atoms simultaneously closing detection and locality loopholes. *Phys. Rev. Lett.*, 119:010402, Jul 2017.

[24] N. Schlosser, G. Reymond, and P. Grangier. Collisional blockade in microscopic optical dipole traps. *Phys. Rev. Lett., 89:023005*, 2002.

[25] V.Andreev. Doppler-shift suppression for one-photon transition in the hydrogen experiment. In *Ringberg Seminar*, 2017.

[26] J. Volz. *Atom-Photon Entanglement*. PhD thesis, 2006.

[27] M. Weber. *Quantum optical experiments towards atom-photon entanglement*. PhD thesis, 2005.

[28] M. Zukowski, A. Zeilinger, M. A. Horne, and A. K. Ekert. Event-ready-detectors" bell experiment via entanglement swapping. *Phys. Rev. Lett., 71*, 1993.

Danksagung

An dieser Stelle möchte ich mich bei allen bedanken, die zum Gelingen dieser Arbeit beigetragen haben:

- Professor Harald Weinfurter für die Aufnahme in seine Arbeitsgruppe und die angenehme und freie Arbeitsatmosphäre.

- Dr. Wenjamin Rosenfeld für seine außerordentliche Hilfsbereitschaft bei offenen Fragen und für die vielen physikalischen Diskussionen.

- Robert Garthoff für seine ausgezeichnete Betreuung während der gesamten Masterarbeit und für die vielen physikalischen Diskussionen und die Zeit im Labor.

- Kai Redeker dafür, dass er immer ein offenes Ohr für Fragen hatte und für seinen hervorragenden Musikgeschmack im Labor.

- Tim van Leent für die lustige Zeit bei Konferenzen.

- Martin Zeitlmaier, dass er mich in seinem Büro aufgenommen hat.

- Allen Mitglieder der Arbeitsgruppe Weinfurter für die schöne gemeinsame Zeit.

- Bei allen meinen Freunden für die lustige Zeit während des Physikstudiums, vor allem bei Stefan, Bas, Margret, Paul, Anna, Pascal und Johanna.

- Bei meinen Eltern und meinen Geschwistern für die nie endende Unterstützung.

Selbstständigkeitserklärung:

Hiermit erkläre ich, die vorliegende Arbeit selbständig verfasst zu haben und keine anderen als die in der Arbeit angegebenen Quellen und Hilfsmittel benutzt zu haben.

München, den 02. Oktober 2018

....
(Timon Hummel)